Quantitative Analysis of 3D Tissue Deformation Reveals Key Cellular Mechanism Associated with Initial Heart Looping

AUTHOR(S):

Kawahira, Naofumi; Ohtsuka, Daisuke; Kida, Naoki; Hironaka, Ken-ichi; Morishita, Yoshihiro

CITATION:

Kawahira, Naofumi ...[et al]. Quantitative Analysis of 3D Tissue Deformation Reveals Key Cellular Mechanism Associated with Initial Heart Looping. Cell Reports 2020, 30(11): 3889-3903.e5

ISSUE DATE:

2020-03-17

URL:

http://hdl.handle.net/2433/250778

Article

Cell Reports

Quantitative Analysis of 3D Tissue Deformation Reveals Key Cellular Mechanism Associated with Initial Heart Looping

Graphical Abstract

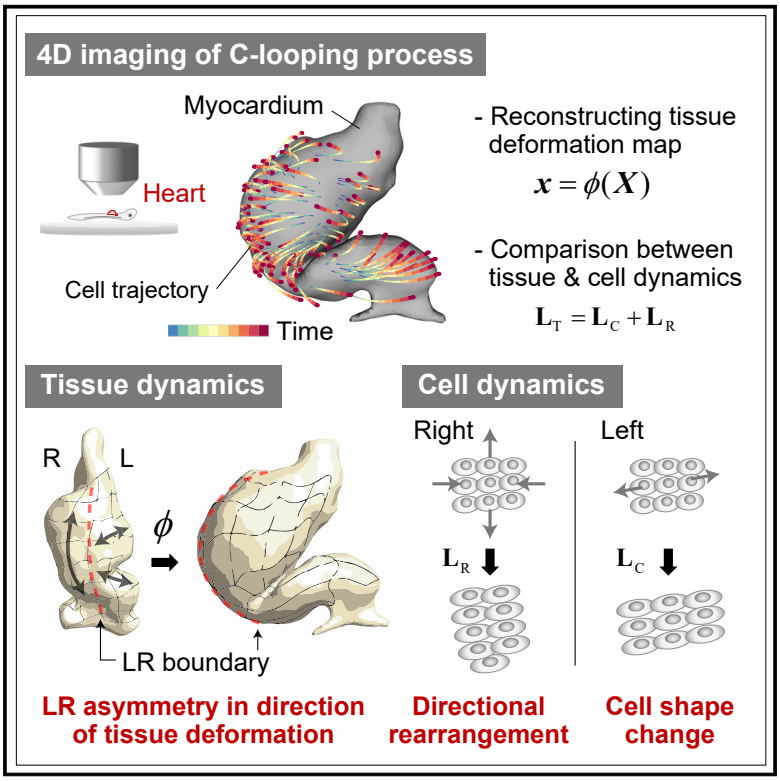

Authors

Naofumi Kawahira, Daisuke Ohtsuka, Naoki Kida, Ken-ichi Hironaka, Yoshihiro Morishita

Correspondence

daisuke.ohtsuka@riken.jp (D.O.), yoshihiro.morishita@riken.jp (Y.M.)

In Brief

Kawahira et al. reveal that initial heart looping is achieved by left-right (LR) asymmetry in the direction of tissue deformation, originating from right-specific directional cell rearrangement. These findings demonstrate that heart looping involves dynamic/intrinsic cellular behaviors within tubular tissue itself, providing a significantly different viewpoint from previous models focusing on LR asymmetry in growth and/or stress at tube boundaries.

Highlights

- Quantifying tissue and/or cell dynamics is essential for revealing morphogenetic mechanisms
- Initial heart looping is achieved by left-right asymmetry in the direction of tissue deformation
- The tissue-scale asymmetry is caused by right-specific directional cell rearrangement
- The directional cell rearrangement occurs in a F-actin-dependent manner

Kawahira et al., 2020, Cell Reports *30*, 3889–3903
March 17, 2020
https://doi.org/10.1016/j.celrep.2020.02.071

CellPress

Cell Reports
Article

Quantitative Analysis of 3D Tissue Deformation Reveals Key Cellular Mechanism Associated with Initial Heart Looping

Naofumi Kawahira,[1,2] Daisuke Ohtsuka,[1,*] Naoki Kida,[1] Ken-ichi Hironaka,[3] and Yoshihiro Morishita[1,4,5,*]
[1]Laboratory for Developmental Morphogeometry, RIKEN Center for Biosystems Dynamics Research, Kobe 650-0047, Japan
[2]Department of Anatomy and Cell Biology, Graduate School of Medicine, Kyoto University, Yoshida-Konoe-cho, Sakyo-ku, Kyoto 606-8501, Japan
[3]Department of Biological Sciences, Graduate School of Science, The University of Tokyo, Tokyo 113-0033 Japan
[4]Precursory Research for Embryonic Science and Technology (PRESTO) Program, Japan Science and Technology Agency, 4-1-8 Honcho, Kawaguchi, Saitama 332-0012, Japan
[5]Lead Contact
*Correspondence: daisuke.ohtsuka@riken.jp (D.O.), yoshihiro.morishita@riken.jp (Y.M.)
https://doi.org/10.1016/j.celrep.2020.02.071

SUMMARY

Despite extensive study, the morphogenetic mechanisms of heart looping remain controversial because of a lack of information concerning precise tissue-level deformation and the quantitative relationship between tissue and cellular dynamics; this lack of information causes difficulties in evaluating previously proposed models. To overcome these limitations, we perform four-dimensional (4D) high-resolution imaging to reconstruct a tissue deformation map, which reveals that, at the tissue scale, initial heart looping is achieved by left-right (LR) asymmetry in the direction of deformation within the myocardial tube. We further identify F-actin-dependent directional cell rearrangement in the right myocardium as a major contributor to LR asymmetric tissue deformation. Our findings demonstrate that heart looping involves dynamic and intrinsic cellular behaviors within the tubular tissue and provide a significantly different viewpoint from current models that are based on LR asymmetry of growth and/or stress at the tube boundaries. Finally, we propose a minimally sufficient model for initial heart looping that is also supported by mechanical simulations.

INTRODUCTION

How organs achieve their specific morphologies during development is a major unsolved question in biology. For example, the heart develops a sophisticated and complex three-dimensional (3D) morphology from a much simpler structure. In higher-vertebrate embryos, heart morphogenesis begins with the formation of a straight heart tube derived from the mesoderm. This tube then undergoes looping, septation, and valve formation concomitant with the fate specification into cardiac muscle and conduction system to create a fully functional four-chambered heart (Moorman and Christoffels, 2003; Hoogaars et al., 2007b; Kirby, 2007).

Among these morphogenetic processes, heart looping is the first event that shows a clear morphological left-right (LR) asymmetry (Patten, 1922; Figures 1A and 1B). In particular, during early phases, the straight heart tube acquires a C-shape (called C-looping), which then becomes more helical (e.g., S-looping) (see, for example, figure 1 of Männer, 2000, in which the electron microscopic images of morphological change during the C-looping process are shown). Such looping has been intensively studied, both experimentally and theoretically. In addition to molecular biology studies (Hoogaars et al., 2007a; Hoogaars et al., 2007b; Evans et al., 2010), cellular- and tissue-scale mechanisms involved in looping also have been examined. Among the many hypothetical models proposed to date (for a review on classical models, see, for example, Shi et al., 2014b), a prevailing model describes the achievement of heart looping through a combination of ventral bending and rightward rotation based on the observation that the ventral midline becomes the outer curvature of C-shaped heart tube (Männer, 2000; Kirby, 2007; Figure 1C, left). In this model, dorso-ventral differences in changes of cell size and/or shape are considered to drive bending of the heart tube in the ventral direction, and subsequent LR asymmetric growth of omphalomesenteric veins (OVs) (i.e., posterior branches) is assumed to drive rightward rigid body rotation of the tube (Shi et al., 2014b). In addition to ventral-bending and rotation components, a contribution of a slight rightward bend was also suggested (Voronov et al., 2004). Another prevailing model is based on physical buckling wherein longitudinal elongation of the heart tube that is physically confined within the pericardial cavity is regarded as the morphogenetic mechanism (Bayraktar and Männer, 2014; Le Garrec et al., 2017). LR asymmetry in cell ingression is included as a boundary condition and is assumed to be a driving force of rightward bending (Figure 1C, right). In this context, both prevailing models assume that LR asymmetry in boundary conditions, i.e., asymmetric growth of or cell ingression at OVs, is the main mechanism by which rightward rotation/bending is achieved. Recent high-resolution imaging using zebrafish embryos by Ocaña et al., 2017 showed LR asymmetry in cell movement around the posterior pole of the

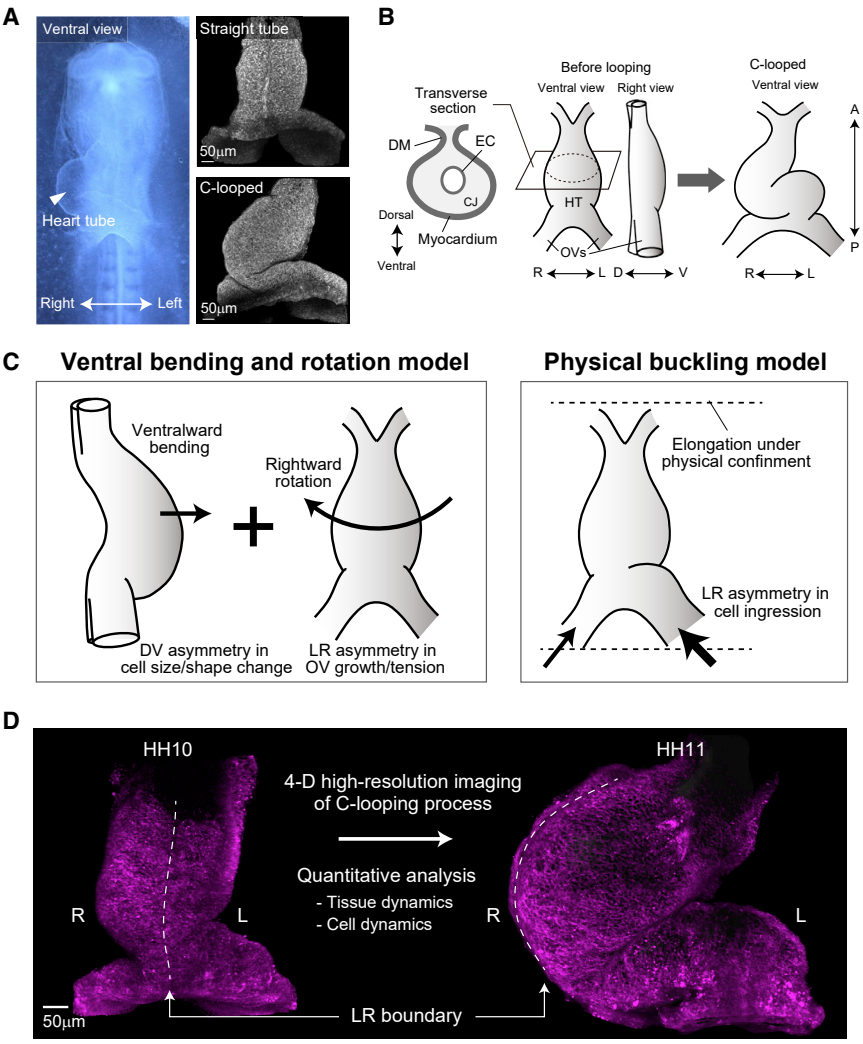

Figure 1. C-Looping of a Developing Chick Heart Tube

(A) A chick embryo at HH11+/12 (left), a straight heart tube before looping (right, top), and C-looped tube (right, bottom).

(B) A schematic representation of the C-looping process. The heart tube is mainly composed of the myocardium, cardiac jelly (CJ), and endocardium (EC).

(C) Two currently prevailing models for C-looping: (left) ventral bending and rotation model and (right) physical buckling model. Both models assume that the left-right asymmetry in the boundary condition, i.e., the asymmetric growth or cell ingression of OVs, is the main mechanism to achieve rightward looping.

(D) A sample used for quantitative analysis of tissue/cell dynamics, illustrating a typical morphological change that we focused on here.

DM, dorsal mesocardium; OV, omphalomesenteric vein.

heart tube, which was suggested to cause the leftward shift of the posterior pole, although how this shift relates to the rightward looping is still unknown.

Importantly, however, the straight heart tubes seen in chick and fish embryos can achieve a C-shaped morphology even under explant cultures (Latacha et al., 2005; Noël et al., 2013), which strongly suggests that this C-looping, an early phase of the entire looping process, occurs not because of boundary conditions (i.e., LR asymmetry at the posterior ends) but instead is an intrinsic morphogenetic process wherein tubular tissue itself should deform/grow non-uniformly rather than a simple elongation along the antero-posterior or longitudinal axis of the heart tube. Thus, in this study, we examined the intrinsic mechanism of C-looping focusing on tissue-level deformation dynamics of the entire heart tube and its relation to local cell dynamics. As pointed out in previous studies (Guirao et al., 2015; Morishita et al., 2017), multiple tissue deformation patterns produce similar changes in morphological appearance. Thus, evaluating proposed models and understanding underlying mechanisms of organ development require precise information about tissue deformation patterns that quantitatively describe the morphogenetic process itself. Furthermore, elucidating whether and to what extent each cellular process, i.e., division/apoptosis, size/shape change, and rearrangement, contributes to tissue-level deformation is essential to identifying which cellular process dominates during morphogenesis of a given organ. As such, quantitative comparative analyses of tissue and cellular dynamics are needed to evaluate the quality of proposed models. In the context of heart looping processes, even though the history of fate mapping studies of the cardiac field spans nearly 100 years, few details concerning tissue-level deformation dynamics and cellular movement within the heart tube that has already formed, rather than simply cell ingression at the tube boundaries, are available. Thus, we could not appropriately evaluate previous models that were based on limited information (e.g., 2D planar observations with low spatial and temporal resolution).

To overcome these issues, we established a 4D (3D space and time) high-resolution live-imaging system to characterize the C-looping process using developing chick embryos. The major advantages of chick embryos over mice are ease of observation and morphological similarity to the human heart tube (Kirby, 2007). In the chick development, C-looping is commonly said to occur during a period from Hamburger and Hamilton (HH) stage 9+/10− to HH11+/12 (Männer, 2000); Figure 1D shows a typical morphological change during this period, and here we focused on the tissue/cell dynamics for this process. Morphological changes after HH12, i.e., more helical shaping including S-looping, are difficult to image at high resolution, which precludes objective discussion of morphogenetic processes. We first reconstructed a 3D tissue deformation map of the heart

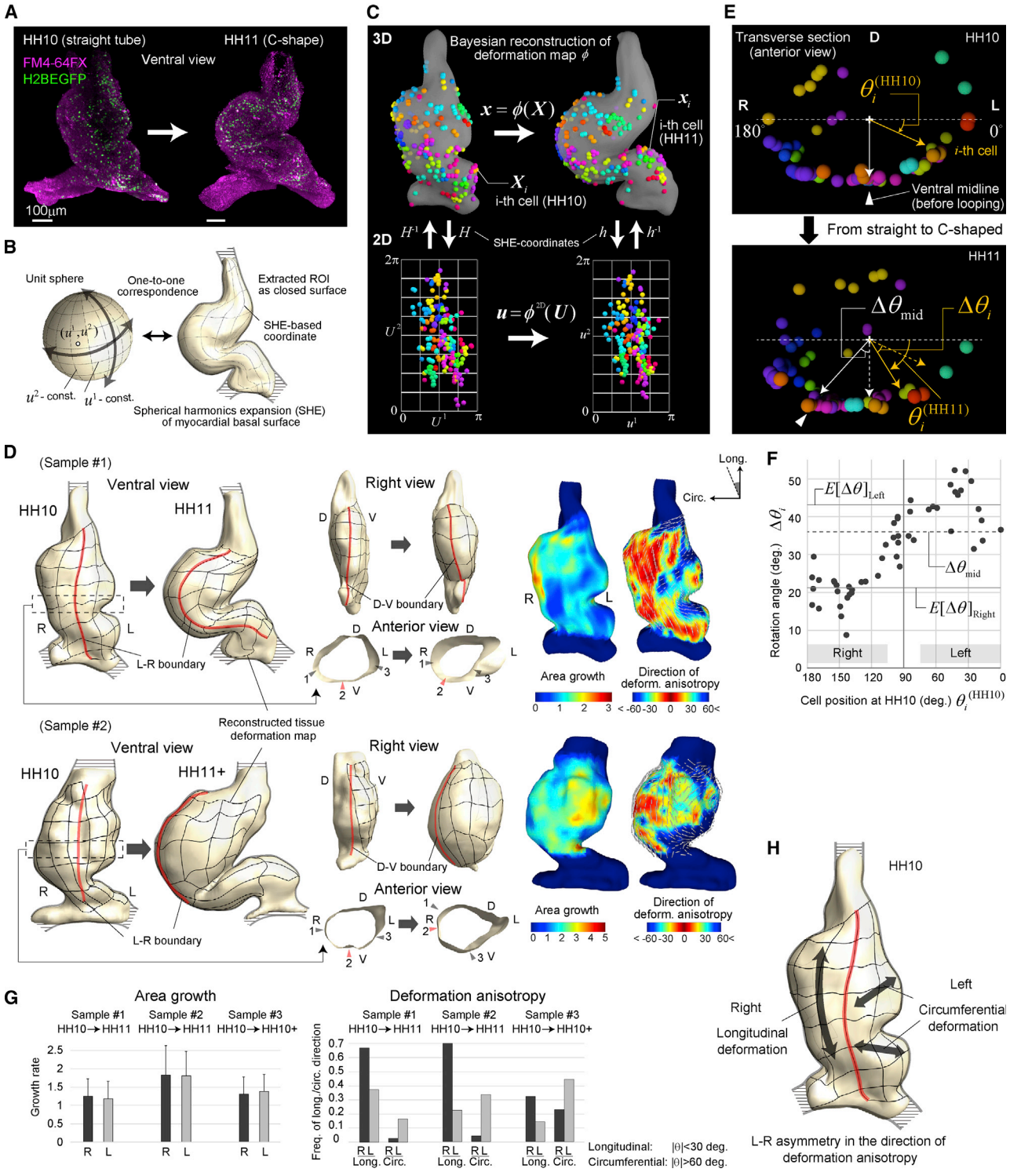

Figure 2. Quantitative Analysis of Tissue Deformation Dynamics

(A) Two-photon microscopy images of heart tube morphology (magenta) and GFP-expressing cardiomyocytes that serve as landmarks for reconstructing a tissue deformation map.

(B) Mathematical description of heart tube morphology using spherical harmonics expansion.

(C) Bayesian reconstruction of tissue deformation map based on the positional changes of a few hundred labeled cells (for details, see Morishita et al., 2017).

(legend continued on next page)

tube during C-looping from cell trajectory data and found that, at the tissue level, the LR asymmetry in the direction of deformation anisotropy within the myocardial tube achieves the C-looping.

We then examined key cellular mechanisms that realize the observed anisotropic tissue deformation. Quantifying cellular dynamics and comparing them with tissue-level deformation patterns, we found that directional cell rearrangement in the right-sided heart tube is the main contributor to the anisotropic tissue deformation for achieving C-looping. Although cell rearrangement was observed long before the looping process in zebrafish embryos (Smith et al., 2008; Lenhart et al., 2013), here we reveal the relationship between cell movement within the formed heart tube and tissue-level deformation. We also show that actin polymerization, rather than myosin phosphorylation, was required for this directional cell rearrangement within the myocardial tube.

Most notably, our findings obtained from high-resolution imaging and quantitative analyses are inconsistent with tissue/cellular behaviors assumed in any previous models and demonstrate that heart looping is realized by much more dynamic and intrinsic cellular behaviors within the entire tube already formed, not at the tube boundaries, than was previously assumed (Rosenquist and DeHaan, 1966; Manasek et al., 1972b). As shown in this study, quantifying the relationship between tissue and cellular dynamics is essential for clarifying and defining the mechanism of complex organ morphogenesis, and the resulting information could be applied to modeling studies to support the plausibility of proposed biological models.

RESULTS

C-Looping Is Achieved through LR Asymmetry in the Direction of Deformation Anisotropy within the Myocardial Tube at the Tissue Level

Quantifying tissue-level deformation dynamics provides essential information needed to understand morphogenetic mechanisms of an entire organ (Guirao et al., 2015; Morishita et al., 2017). To precisely describe the 3D deformation process, 3D morphologies of an entire tissue at different time points must be measured, and positions of a sufficient number of landmarks/cells on the heart tissue must be tracked (at minimum the cell number should allow reconstruction of a tissue deformation map with sufficient precision; Morishita et al., 2017). However, previous works that analyzed heart tube morphogenesis were based on limited data due to imaging techniques that allowed, for example, only planar observations of the positions of several landmarks with low resolution (Voronov et al., 2004; Kidokoro et al., 2008).

Here, we began with 4D imaging at a single-cell resolution and precise reconstruction of a myocardium deformation map during early heart development (from HH10 to HH11/11+) in chick embryos (Figure 1D). We focused on myocardium deformation based on its involvement in heart tube morphogenesis. The tube itself also includes cardiac jelly (CJ) and endocardium (EC) (Kirby, 2007), but looping can occur even following chemical removal of CJ (Baldwin and Solursh, 1989).

Through introduction of fluorescent proteins to the primary heart-forming field (mesodermal cells composing the prospective heart tube) by electroporation, we could visualize several hundred cardiomyocytes (STAR Methods). The 3D positions of these labeled cells and the morphology of a heart tube stained with FM4-64FX lipophilic dye were live imaged by two-photon microscopy every 2 h (Figure 2A; STAR Methods). The trajectories of labeled cells or those of a few cell clusters were extracted using Imaris software. To describe heart tube morphology, we constructed polygonal models of the basal surface of the myocardium (i.e., the boundary between myocardium and CJ) from the microscopy image. Because the myocardial tissue is sufficiently thin (~15 μm or 1–2 cell layers), we here focused on myocardial surface deformation. We will touch on the change in tissue thickness during morphogenesis in a later section on quantification of cellular geometry (see the subsection Changes in Cell Shape and Size Cannot Explain the LR Asymmetry in Tissue Deformation Anisotropy).

To reconstruct the deformation map of the myocardium surface, we first defined 2D coordinate systems on the curved surface at each time point using spherical harmonics expansion (SHE) (Shen et al., 2009; Figure 2B), which allows the approximation of arbitrary surfaces as a closed surface defined by a series of harmonic functions. The SHE representation facilitates analytical treatment of surfaces having a complex morphology. For example, the metric tensor needed to reconstruct the tissue deformation map can be readily calculated at arbitrary points on the curved surface. Using SHE-based coordinates, we specified the positions of fluorescently labeled cells on the tissue at each stage. From these data for both 2D and 3D representations of heart tube morphology and landmark positions, we reconstructed deformation dynamics of myocardial tissue using our previously reported Bayesian method (Morishita et al., 2017; Figures 2C and S1A). Because the heart tube adheres to the dorsal mesocardium at its dorsal midline during this stage (Figure 1B), we reconstructed the map for about two-thirds of the ventral surface.

We first checked the accuracy of the reconstructed map by evaluating the prediction error in cross-validation; the mean error of the map was about 10 μm, which indicates sufficient accuracy (Figure S1B). As shown by the electron microscope images

(D) Left: reconstructed tissue deformation maps for two embryos (the ventral and right views are shown). Right: the spatial patterns of area growth rate and deformation anisotropy.
(E) Measurement of the rotation angle of each cell on the transverse cross-section of the heart tube around the central axis of the tube (sample 1).
(F) Quantified rotation angle in Figure 2E. If the heart tube indeed undergoes rigid body rotation, all of the cells on the tube should show the same or a similar rotation angle. However, the cells that were initially included in the right-sided tissue showed much smaller rotation angles than those for cells in the original left-sided tissue. $E[\Delta\theta]_{\mathrm{Left}}$ and $E[\Delta\theta]_{\mathrm{Right}}$ are the average rotation angles of left and right tissues, respectively, and $\Delta\theta_{\mathrm{mid}}$ is the rotation angle of the ventral midline.
(G) Left: comparison of mean area growth rate between left and right tissues in three embryos. Error bars represent the standard deviation. Right: comparison of the direction of tissue deformation anisotropy between left and right tissues; the frequencies of longitudinal ($|\theta| < 30^\circ$) and circumferential ($|\theta| > 60^\circ$) directions are shown.
(H) Summary of tissue deformation analysis. At the tissue level, C-looping is achieved by left-right asymmetry in the direction of deformation anisotropy.

(Männer, 2000), the LR boundary of the heart tube shifts rightward and shows a C-shape (Figure 2D). Before considering in detail the spatial patterns of local deformation characteristics that can be calculated from the reconstructed map, we can readily learn several important facts from movies showing the trajectories of landmark cells (see Videos S1, S2, and S3), which were made using a simple linear interpolation of raw trajectory data along the time axis. First, the movies from the ventral, right, and anterior views show that the heart tube undergoes very little ventral bending (i.e., bending on the original midsagittal plane) (Videos S1 and S2). Second, the movie from the anterior view (Video S3) shows that the heart tube appears to be rotating. We measured the rotation angle of each cell around the central axis of the tube after aligning the axis position for all time points (Figures 2E and 2F). As a result, rotation of the tube did occur, but interestingly we found that the amount of rotation was clearly different between the tissues on the left and right side of the tube, meaning that the observed cell movement cannot be explained by a simple rigid body rotation. If the heart tube indeed undergoes rigid body rotation, all of the cells on the tube should show the same or a similar rotation angle. However, the cells that were initially included in the right-sided tissue showed much smaller rotation angles than those for cells in the original left-sided tissue. As shown below, this LR asymmetry in the rotation angle arises from the clear differences in tissue deformation between the left- and right-sided tissues, which has not been assumed in previous models of C-looping. Further, the rightward shift in the LR boundary and the apparent rotation of the tube are due to the large deformation that the heart tube itself (rather than the boundaries) undergoes. It should be noted that evaluation of whether the tube undergoes rigid body rotation or large deformation of itself does not depend on the choice of axis on which to measure the amount of rotation (Figure S1C).

To observe tissue deformation in greater detail, we next calculated the spatial patterns of local deformation characteristics (i.e., area growth rate and deformation anisotropy) (Figures 2D, right; Figure S1E; STAR Methods). Our observations and previous reports about expression patterns of heart development-related genes (Kathiriya and Srivastava, 2000; Moorman and Christoffels, 2003) highlight the importance of differences in the LR behavior, and thus we compared the mean values of the deformation characteristics between left- and right-sided tissues (Figure 2G). There was little difference between the left and right tissues in terms of area growth rate, and thus the contribution of area growth pattern to C-looping would not dominate. In contrast, deformation anisotropy showed a clear LR difference that can directly explain the C-looping process. The left tissue deforms in a more circumferential direction, whereas the right tissue deforms in a more longitudinal direction (Figures 2G and 2H). Thus, the LR boundary of the heart tube shifts rightward by anisotropic deformation of the left tissue in a circumferential direction. Furthermore, because the right tissue deforms along the longitudinal axis, the position of the dorsal-ventral boundary is almost unchanged when the C-shaped tube is first observed (see the reconstructed tissue deformation map of sample 1 shown in the top panels of Figure 2D). In a later phase of C-looping, as reported in many previous studies, the LR boundary (or original ventral midline) forms the outer curve of the tube, and the original right dorsal-ventral boundary shifts to the more dorsal side (see the result of sample 2 shown in the lower panels of Figure 2D). Further, the LR asymmetry in the direction of tissue deformation becomes significant in a later phase; in fact, in sample 3, where the tissue deformation from HH10 to HH10+ was analyzed (Figure 2G; Figure S1E), the LR asymmetry of deformation direction is less clear compared with samples 1 and 2.

Taken together, the tissue deformation analysis showed that initial heart looping (i.e., morphological change from a straight tube to a C-shaped tube with the outer curvature turned to the right) is not achieved through spatial heterogeneity of the surface area change, but instead by the LR asymmetry in the direction of deformation anisotropy within the myocardial tube, and specifically through circumferential and longitudinal elongation of the left and right tissues, respectively. This finding differs from behaviors assumed in previously proposed models.

Cell Division Is Not Involved in C-Looping

Quantitative analysis of tissue-level deformation revealed the importance of the direction of deformation for C-looping. In principle, different cellular processes, including cell division, cell death, cell shape/size change, and cell rearrangement, can affect tissue deformation and anisotropy (Blanchard et al., 2009), although which of these processes significantly contributes to heart tube C-looping is unclear. Previous studies using chick embryos reported that, during early development, the rates of cell division or apoptosis are low within the heart tube and occur with no clear LR asymmetry, and that changes in cell number through cell division are likely not a major factor in morphogenesis (Stalsberg, 1969; Soufan et al., 2006). To assess the effects of cell division on heart tube C-looping, we examined changes in C-looping in the presence of the cell division inhibitor aphidicolin. We found that, even in the presence of cell division inhibition, C-looping still occurred (Figure S2; STAR Methods), which suggests that cell division (including its rate and orientation) is not a driver of C-looping.

In the context of mouse heart development, a previous study that performed clonal analysis indicated that cell division orientation could be spatially biased and thus could be a candidate factor that affects morphogenesis (Meilhac et al., 2004). However, in that report, the focal stage was much later than the C-looping stage. Moreover, cell positions at two (or more) different time points cannot be directly compared in clonal analysis, and thus the result in that report does not necessarily indicate that observed relative positions of daughter cells were determined by the orientation of division because the relative positions are also significantly influenced by cell rearrangement.

Changes in Cell Shape and Size Cannot Explain the LR Asymmetry in Tissue Deformation Anisotropy

As mentioned above, changes in cell shape and size are currently regarded as a prime cellular mechanism involved in C-looping. To date, several studies reported that cell size and shape changes occur during the looping process (Manasek et al., 1972b; Soufan et al., 2006; Auman et al., 2007). From a modeling perspective, other studies performed continuum mechanical simulations to explain the bending mechanism of the heart tube based on the assumptions that cell shape changes actively occur and/or differential hypertrophic growth between

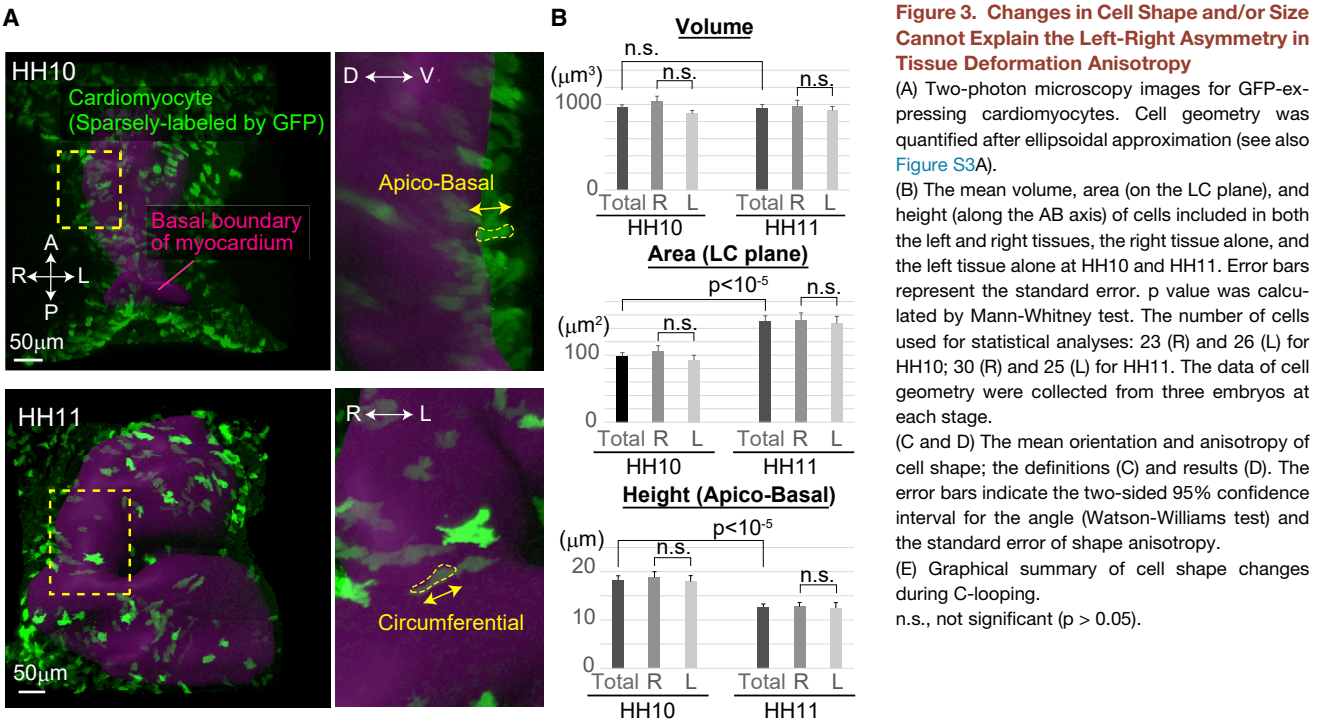

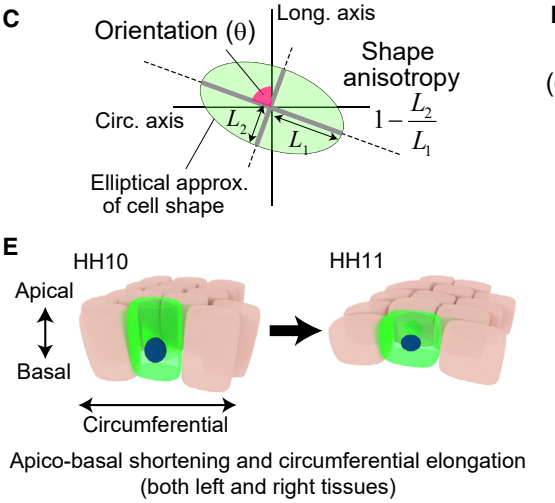

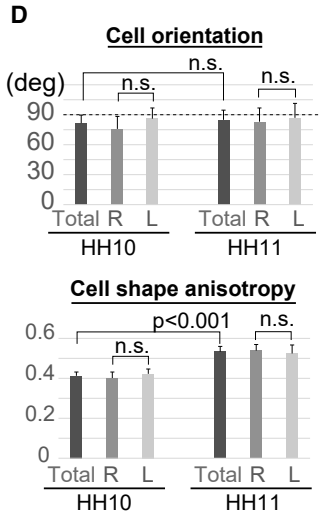

Figure 3. Changes in Cell Shape and/or Size Cannot Explain the Left-Right Asymmetry in Tissue Deformation Anisotropy

(A) Two-photon microscopy images for GFP-expressing cardiomyocytes. Cell geometry was quantified after ellipsoidal approximation (see also Figure S3A).

(B) The mean volume, area (on the LC plane), and height (along the AB axis) of cells included in both the left and right tissues, the right tissue alone, and the left tissue alone at HH10 and HH11. Error bars represent the standard error. p value was calculated by Mann-Whitney test. The number of cells used for statistical analyses: 23 (R) and 26 (L) for HH10; 30 (R) and 25 (L) for HH11. The data of cell geometry were collected from three embryos at each stage.

(C and D) The mean orientation and anisotropy of cell shape; the definitions (C) and results (D). The error bars indicate the two-sided 95% confidence interval for the angle (Watson-Williams test) and the standard error of shape anisotropy.

(E) Graphical summary of cell shape changes during C-looping.

n.s., not significant ($p > 0.05$).

dorsal and ventral sides is the driving force for bending (Latacha et al., 2005; Shi et al., 2014a, 2014b).

We next addressed how changes in cell size and shape align with tissue deformation patterns by quantifying cell geometry and comparing it with the tissue deformation patterns clarified in the previous section (Figure 3; STAR Methods). In all stages that we examined (i.e., from HH10 to HH11), most of the cardiomyocytes had elongated shapes, which we approximated as ellipsoids to quantify geometric characteristics (Figures 3A and S3A). In particular, we compared the characteristics between the left and right sides of the heart tube based on our finding that LR asymmetry of tissue deformation anisotropy is essential for C-looping.

Cell volume was almost unchanged regardless of stage (at least from HH10 to HH11) or position (i.e., left or right), which is consistent with a report by Soufan et al. (2006). In contrast, the cell height along the apical-basal (AB) axis and the cross-sectional cell area on a plane perpendicular to the AB axis and through the cell centroid (subsequently referred to as the longitudinal-circumferential [LC] area) showed clear changes during the period between HH10 and HH11; the height decreased, and the LC area increased on both the left and the right side (Figure 3B). This observation that the longest cell axis is oriented in the direction of the AB axis at HH10 (before C-looping occurs) and on the LC plane at HH11 (during the looping) is consistent with a previous report by Manasek et al. (1972b). Importantly, we saw no clear difference in the values for cell volume, area, height, and their temporal changes from HH10 to HH11 between the left and right tissues.

We then examined the cell orientation and shape anisotropy on the LC plane to compare with the tissue deformation anisotropy quantified in the previous section (Figure 3C). On the LC plane, cells were, on average, oriented in the circumferential direction regardless of stage or position, and the shape anisotropy increased (i.e., elongated circumferentially) from HH10 to HH11 (Figure 3D); again, there was no clear difference in the cell orientation, shape anisotropy, and their temporal changes between the left and right sides of the heart tube during this period (Figure 3E). On the left side, the directions of the tissue deformation

anisotropy and the change in cell shape anisotropy were nearly consistent. In contrast, the longitudinal elongation of the right-sided tissue was nearly perpendicular to the direction of cell shape elongation. Thus, the 3D quantification of cell geometry revealed that changes in cell shape and size have no clear asymmetry between the left and right tissues, and that they are insufficient to explain the tissue deformation patterns observed during C-looping, especially the longitudinal elongation of the right-sided tissue.

Directional Cell Rearrangement within the Myocardial Tube Is a Major Contributor to Longitudinal Deformation of Right-Sided Tissue

To clarify the cellular mechanism that causes longitudinal deformation of the right side of the heart tube, we next focused on cell rearrangement that could achieve anisotropic tissue deformation. In the development of various organs/animals, cell rearrangement has a key role in morphogenesis, as well as cell division/apoptosis and changes in cell shape/size (Davidson and Keller, 1999; Bertet et al., 2004; Nishimura et al., 2012). In the context of heart development, recent advances in live-imaging techniques allowed the observation of cell migration and rearrangement, particularly before and during heart tube formation in zebrafish embryos (Smith et al., 2008; Lenhart et al., 2013; Pestel et al., 2016; Merks et al., 2018). Regarding amniotes, although previous studies reported cell migration and rearrangement in the mesoderm of chick embryos before heart tube formation (Yue et al., 2008; Aleksandrova et al., 2015; Kidokoro et al., 2018), whether and how frequently cell rearrangement occurs and to what extent it relates to tissue-level deformation during 3D morphogenesis, including the C-looping process, is unclear.

To address these questions, we first performed 3D time-lapse imaging at single-cell resolution for a patch of left- and right-sided tissue every 10 min (STAR Methods). Because tracking changes in adjacent relationship between cells based on membrane information was difficult, we instead tracked the nucleus position for each cell in the patch (Figures 4A and S4; Video S4). From this information on nucleus trajectory and data for changes in the average cell shape examined in the previous section, we quantified the contribution of cell rearrangement to tissue deformation during morphogenesis that occurs between HH10 and HH11 by using a tensor decomposition method proposed by Blanchard et al. (2009). In their method, cell rearrangement is measured by the tensor that is defined as the difference between two kinds of tensors, $\mathbf{L}_T$ and $\mathbf{L}_C$, which we denote by $\mathbf{L}_R$ ($= \mathbf{L}_T - \mathbf{L}_C$); $\mathbf{L}_T$ is the tissue velocity gradient tensor that represents the deformation per unit time as a cell population (or as a continuum), and $\mathbf{L}_C$ is the cell shape strain rate tensor that represents the change in cell shape. $\mathbf{L}_R$ reflects the continuous sliding of the bulk of neighboring cells past each other. The local rate and principal directions of sliding can be directly derived from $\mathbf{L}_R$. We calculated $\mathbf{L}_T$ from time-lapse imaging data showing the trajectories of nuclei included in the focal patch. Our high-resolution imaging allowed direct observation of a cell population that shows gradual anisotropic deformation of the right- and left-sided tissues along the longitudinal axis and more circumferential axis, respectively (Figure 4B, green and gray). Meanwhile, we calculated $\mathbf{L}_C$ from information for the average cell shape on the left- and right-sided tissue obtained in the previous section (STAR Methods).

Figures 4C–4F show the calculated contributions of cell rearrangement and cell shape change to the tissue deformation. For the right-sided tissue, along the direction of maximum tissue stretch, which was almost longitudinal (Figure 4D, top), the contribution of cell rearrangement is significantly (about three times) larger than that of cell shape change (Figures 4C, left, and 4D). On the other hand, in the circumferential direction, the tissue has minimal deformation (Figures 4C, right, and 4D, top), which was shown to be achieved by canceling out the circumferential elongation of cell shape through cell rearrangement (Figures 4C, right, and 4D). In this manner, the longitudinal elongation of the right side of the heart tube was achieved mainly by directional cell rearrangement within the tube (in Figures 4A and S4 and Video S4, we can also see the longitudinal elongation of tissue patches through changes in the spatial relationship of multiple adjacent cells). In contrast, as stated earlier, the direction of maximum tissue stretch of the left-sided tissue is more circumferential, and cell shape change rather than rearrangement significantly contributes to the tissue deformation (Figures 4E and 4F). These findings demonstrate that C-looping is realized by much more dynamic cellular behaviors (especially in the right-sided tissue) than was previously assumed, and these behaviors could be elucidated using high-resolution imaging and quantitative analyses.

Actin Polymerization Is Required for Directional Cell Rearrangement that Causes Longitudinal Deformation of Right Tissue

Cell rearrangement is widely observed during organ/animal developmental processes, and acto-myosin activity is often involved (Guillot and Lecuit, 2013). During early heart development, inhibition of actin polymerization abolishes looping (Manasek et al., 1972a; Ghaskadbi and Mulherkar, 1984; Itasaki et al., 1991; Latacha et al., 2005). However, the role of myosin function in looping remains controversial because several studies reported a role for myosin II phosphorylation in C-looping (Lu et al., 2008; Noël et al., 2013; Ocaña et al., 2017), whereas others saw no effect (Latacha et al., 2005; Nerurkar et al., 2006; Shi et al., 2014b). Our replication experiment indicated that myosin phosphorylation does not play a role in C-looping of chick embryos (STAR Methods). Thus, in the following, we examined the role of actin polymerization for the achievement of C-looping.

In previous studies, the requirement for actin polymerization during C-looping was demonstrated only by observing changes in morphological appearance when actin polymerization was inhibited. Even in our replication study, with the treatment of actin polymerization inhibitor (cytochalasin D or latrunculin A was added to embryos at HH10), no looping was observed; in particular, there is no clear LR asymmetry in the heart tube morphology with the wider width and shorter length of tube compared with normal development (Figure 4G; STAR Methods).

To characterize events at cell and tissue levels in the presence of actin-polymerization inhibition, we performed quantitative analyses of tissue and cellular dynamics as done for the normal

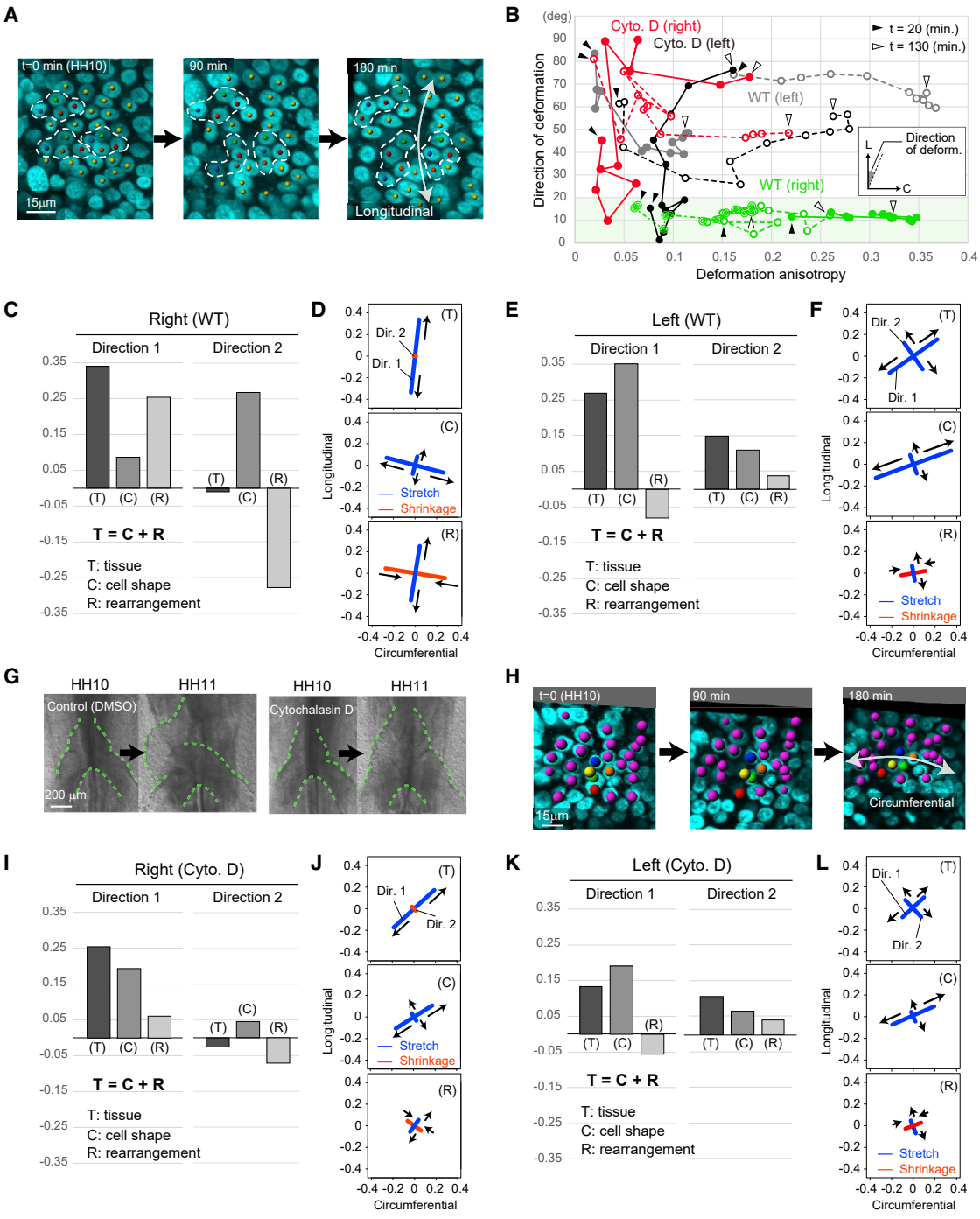

Figure 4. Longitudinal Deformation of Right-Sided Tissue Is Achieved Mainly through F-Actin-Dependent Directional Cell Rearrangement

(A) Time-lapse imaging at a single-cell resolution for a patch (composed of around 30 cells) of right-sided tissue during normal development. Cardiomyocytes surrounded by the white broken lines show rearrangement.

(B) Temporal changes in the magnitude and direction of deformation anisotropy of focal patches. Values taken every 10 min are plotted. Green: right tissue for normal development (n = 3 patches); gray: left, normal (n = 2); red: right tissue under cytochalasin D (CytoD) treatment (n = 2); black: left, cytochalasin (Cyto.) D (n = 2).

(C, E, I, and K) Contributions of cell rearrangement and cell shape change to the tissue strain rate in the right-sided (C) and left-sided (E) tissues during normal development, and in the right-sided (I) and left-sided (K) tissues under CytoD treatment.

(D, F, J, and L) The direction and magnitude of tissue strain rate, symmetrical cell shape strain rate, and strain rate for cell rearrangement during normal development (D, right; F, left) and under CytoD treatment (J, right; L, left).

(G) CytoD treatment inhibits C-looping.

(H) Time-lapse imaging every 10 min at a single-cell resolution for a patch of right-sided tissue treated with CytoD.

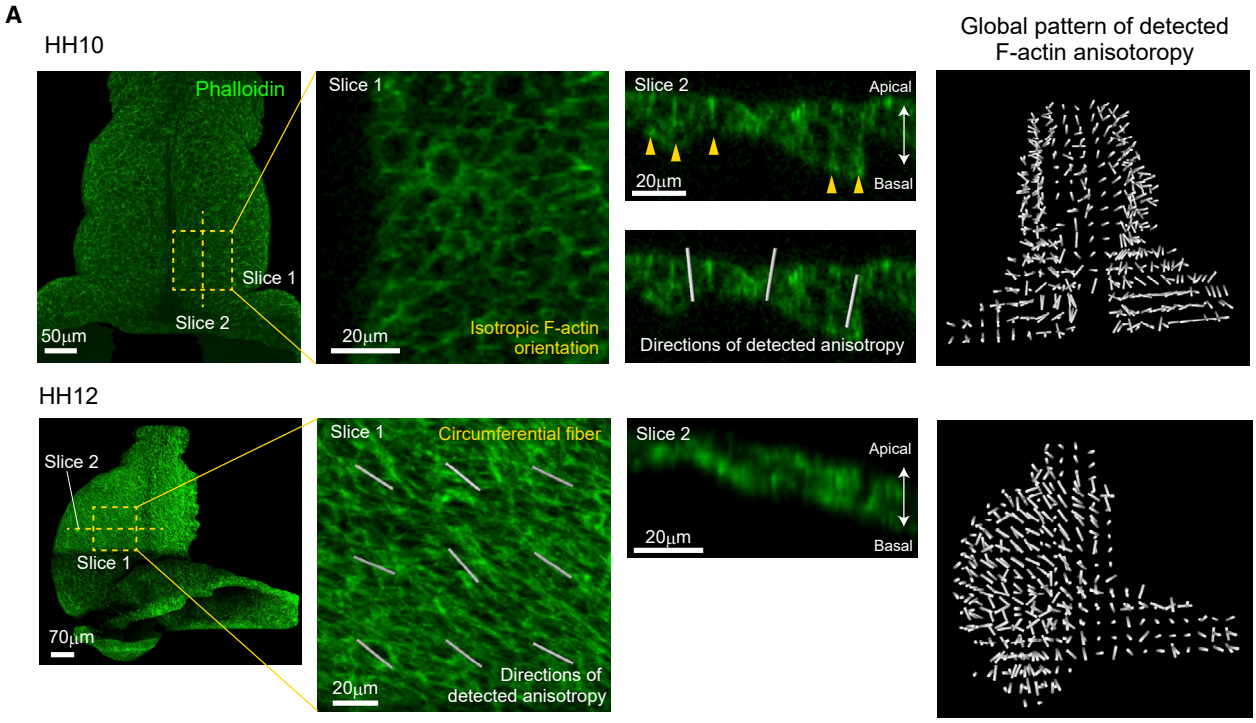

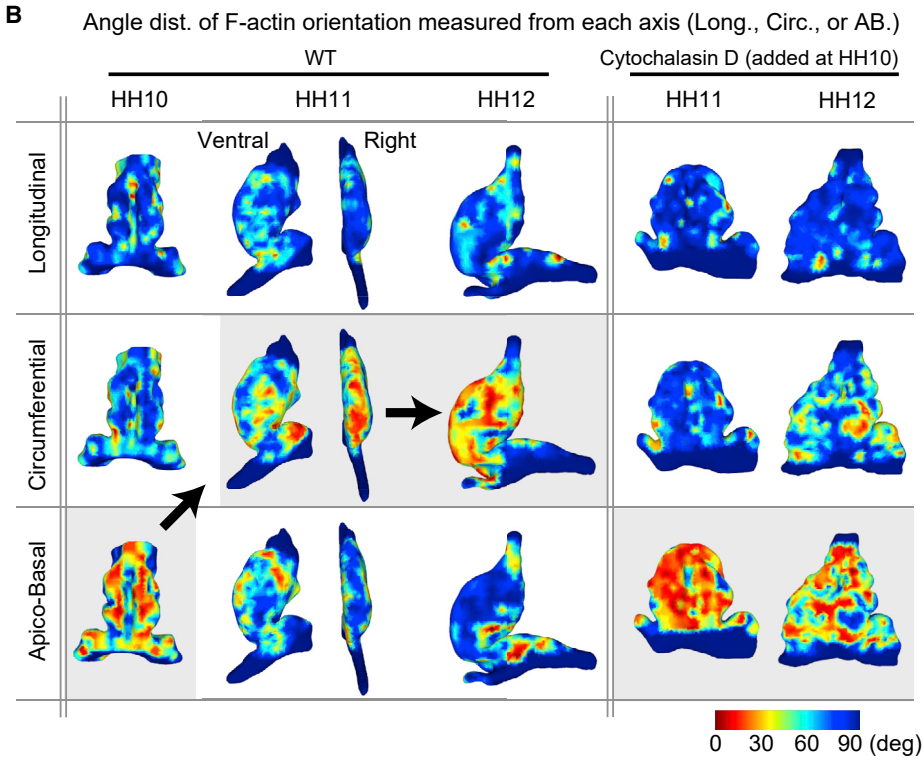

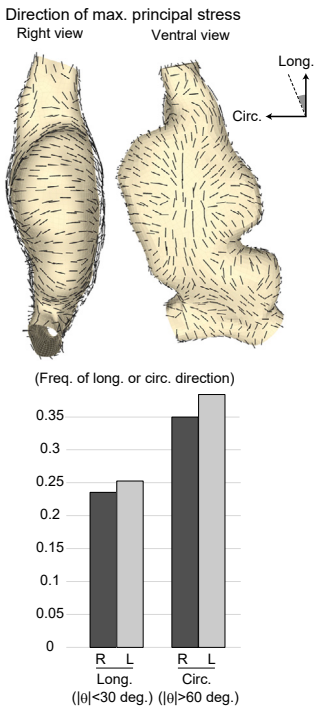

(legend on next page)

development in the previous sections. Red and black lines in Figure 4B show the temporal changes in the magnitude and direction of tissue deformation anisotropy of the right- and left-sided tissues, respectively, that were calculated from time-lapse imaging of cells in a ~30-cell patch under actin-polymerization inhibition by cytochalasin D (Figure 4H; Video S5). These analyses show that the direction of deformation anisotropy in the right-sided tissue was more ambiguous, not oriented in a specific direction, compared with the normal case, resulting in the disappearance of clear LR asymmetry. Regarding cell shape in both the left- and right-sided tissues, as seen in the normal case, the cell height decreased, whereas the LC area enlarged, with cell elongation in the circumferential direction between HH10 and HH11, although the degree of cell elongation was somewhat decreased (Figure S3B). To clarify the relationship between tissue deformation and cellular behaviors under actin polymerization inhibition, we next calculated the three tensors, $\mathbf{L}_T$, $\mathbf{L}_C$, and $\mathbf{L}_R$ (Figures 4I–4L). We observed clear differences from normal development for the right-sided tissue: the contribution of cell rearrangement much decreased and tissue deformation was mostly due to changes in cell shape (Figure 4I, left). Although for the left-sided tissue, the relative contributions of cell rearrangement and cell shape change to the tissue deformation are similar to those during normal development. As a consequence, the direction of tissue deformation of the right-sided tissue was more circumferential in the presence of actin polymerization inhibition (Figure 4J, top), leading to a wider and shorter heart tube. Taken together, these results demonstrated that longitudinal deformation of right-sided tissue promoted by F-actin-dependent directional cell rearrangement is critical to achieving heart tube C-looping.

How Is Directional Information Provided within the Myocardium?

As seen above, during heart development, tissue and cellular dynamics show clear anisotropy (i.e., directional specificity). During C-looping (specifically, from HH10 to HH11), cells in the left-sided tissue elongate in a circumferential direction that is consistent with the tissue-level deformation anisotropy. In contrast, in the right-sided tissue, F-actin-dependent cell rearrangement causes tissue elongation along the longitudinal axis, whereas the cells themselves elongate in a circumferential direction as seen for left-sided tissue. What provides such directional information? Currently, we have no clear answer, but we here show our ideas with tissue mechanical simulations.

First, we need to touch the fact that the orientation of F-actin also shows anisotropy. Previous studies documented that the orientation of F-actin is globally aligned in the circumferential direction during C-looping (e.g., HH11), but no clear pattern can be observed before looping (Itasaki et al., 1989). Because these findings were obtained from 2D observations (i.e., on the LC surface), here we re-examined the spatio-temporal pattern of F-actin orientation in a 3D setting using two-photon imaging (Figure 5A; STAR Methods). Our 3D imaging/analysis revealed that during both HH10 and HH11, F-actin was clearly oriented over the whole heart tube, but its direction depended on the stage; during HH10, F-actin orientation is almost isotropic on the LC plane and relatively biased along the AB axis, whereas during HH11, it was oriented along the circumferential axis (Figures 5A and 5B, left). There was no clear difference in the direction between the left- and right-sided tissues. This dynamic change in F-actin orientation is consistent with the observed changes in cell shape; the long axis of cardiomyocyte is oriented in the AB axis at HH10 and the circumferential direction at HH11, respectively (Figure 3). In the presence of cytochalasin D (added at HH10), where the heart tube shows no looping (Figure 4G), the F-actin orientation was still biased to the AB (not circumferential) direction at HH11, yet it had a more aggregated (or granulated) state (Figure 5B, right; Latacha et al., 2005), whereas the cell shape was elongated in the circumferential direction (Figure S3B). This result suggests that cell shape changes during C-looping are not necessarily regulated by actin polymerization, and that the F-actin oriented along the circumferential axis plays a key role in the achievement of longitudinal tissue deformation through directional cell rearrangement.

As shown above, cell shape and F-actin orientations in normal development have the same tendencies in that they both orient in the circumferential direction at HH11 and show no clear LR asymmetry. Both cell shape and F-actin are globally oriented across the heart tube, suggesting that local signaling does not determine those orientations. Instead, morphogens and tissue stress could be candidate factors that provide global information to orient cell shape and F-actin. Considering the relevance of stress to the orientation of actin fibers observed in various systems, including cell culture (Pellegrin and Mellor, 2007), developing tissues (Wozniak and Chen, 2009), and mature blood vessels (Yuan and He, 2012), here we focused on the ability of tissue stress to affect the orientations of tissue/cellular/molecular dynamics. The depth of the heart tube precludes simple measurement of stress *in vivo* by external operations such as laser ablation, so we instead estimated stress distribution within the myocardium using continuum mechanical simulations. The C-shaped morphological changes seen in isolated heart tubes suggest that external forces acting on both ends of the heart tube are not essential to the deformation. Thus, for our simulations, we assumed that stress within the myocardium is generated though the hydrostatic pressure from interior substances (e.g., CJ or any type of body fluid) acting in the normal (i.e., the AB axis) direction of myocardium. As a constitutive law representing physical properties of the heart tube, we assumed the hyperelasticity that is often adopted in the mechanical simulations of both matured and developing tissues (Conte et al.,

Figure 5. F-Actin Orientation Dynamics and Tissue Stress as a Candidate Factor that Provides Directional Information to the Myocardium

(A) Extraction of F-actin orientation.

(B) The angle distribution of F-actin orientation measured from each reference axis during normal development (left) and in the presence of cytochalasin D (right).

(C) The distribution of the directions of maximum principal stress (tensile stress) generated by mechanical simulation (top). The directions are biased to the circumferential orientation in both left and right tissues (bottom).

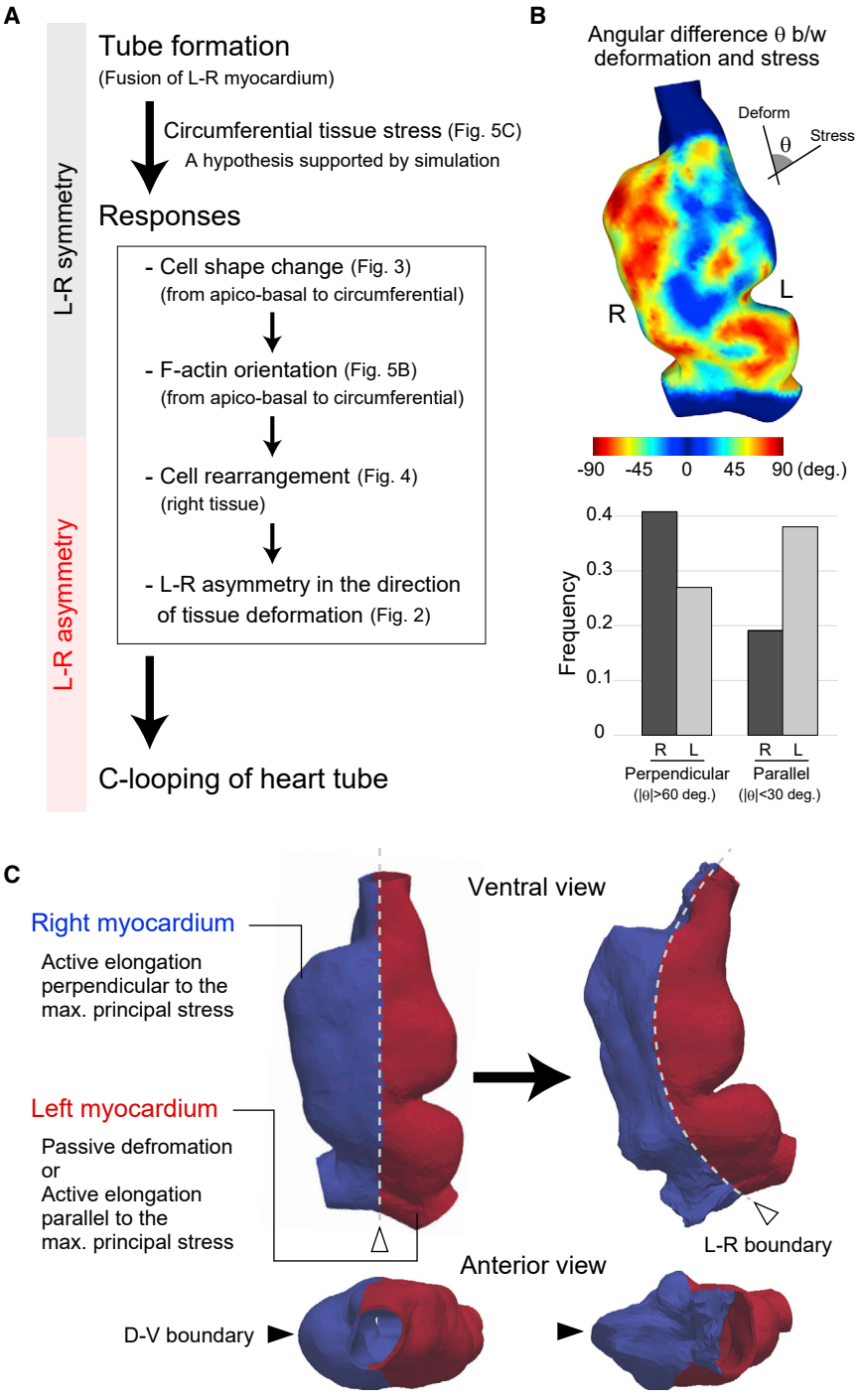

Figure 6. A Working Hypothesis for Heart Tube C-Looping

(A) Summary of this study (see the subsection A Hypothetical Model: Left-Right Asymmetric Response to Tissue Stress Drives C-Looping).

(B) Angular difference between the directions of tissue deformation anisotropy calculated from imaging data and of the maximum principal stress generated by mechanical simulation.

(C) A continuum mechanical simulation with stress-dependent active deformation.

2008; Ambrosi et al., 2011; Savin et al., 2011; Kida and Adachi, 2015; Tallinen et al., 2016; STAR Methods). The myocardium was modeled as a thick-walled 3D tubular structure based on the measured 3D morphology at HH10 (Figure S5).

Figure 5C shows the distribution of the directions of the maximum principal stress. On average, both left- and right-sided tissues undergo circumferential tensile force. This is consistent with the fact that the cell shape and F-actin come to orient along the circumferential axis during the period from HH10 to HH11, and suggests that the tissue stress (i.e., the direction of the maximum principal stress) determines cell shape and F-actin orientation. Furthermore, based on results with cytochalasin D wherein F-actin fails to orient in a circumferential direction, we speculate that F-actin can detect the direction of tissue stress.

A Hypothetical Model: LR Asymmetric Response to Tissue Stress Drives C-Looping

A comprehensive consideration of experimental results and data analyses on tissue/cell dynamics, as well as stress distribution obtained from mechanical simulations, suggests the hypothesis that LR asymmetric response to tissue stress drives C-looping. The following proposed mechanism could thus produce C-looping (Figure 6A). First, when the heart tube is formed at HH9+/10−, tensile stress is generated along the circumferential axis in the myocardium (Figure 5C). Second, this promotes cell elongation in the direction of the stress (Figure 3). Third, simultaneously, through the actin polymerization-depolymerization process, F-actin, which was oriented in the AB direction immediately after tube formation, is re-organized in the circumferential direction (Figure 5B), where the tensile stress is applied (Figure 5C). This process can be interpreted as the detection of the direction of maximum principal stress by F-actin. Fourth, difference in the response to stress between the left- and right-sided tissues leads to cell rearrangement against the tissue stress only in the right-sided tissue. This results in longitudinal elongation of the right-sided tissue, and thus heart tube C-looping.

According to this proposed mechanism, the direction of tissue deformation should be consistent with that of the maximum

principal stress (i.e., the maximum stretching) on the left-sided tissue, and in contrast, the direction of deformation and the maximum principal stress should be perpendicular on the right-sided tissue. Figure 6B shows the angular differences at each position of the myocardium between the anisotropy of tissue deformation obtained from experimental data (Figures 2C and 2G) and stress obtained from simulations (Figure 5C). As expected, there is a clear difference between the left- and right-sided tissues; the angular difference is smaller (19 degrees on average) on the left and is nearly orthogonal (108 degrees) on the right. This tendency is clearer in the anterior half of the tube.

To support this concept, we further performed morphogenetic simulations based on the above hypothesis, i.e., stress-dependent active deformation of right-sided tissue. Because development of continuum models that tolerate 3D large deformations that occur through active deformation and growth is challenging, here we simulated only the initiation of C-shaping (Figure 6C). In the model, we adopted the constitutive law that the right-sided tissue actively elongates perpendicular to the direction of maximum principal stress originating from hydrostatic pressure within the heart tube, whereas the left-sided tissue actively elongates parallel to the stress, but at a much slower rate compared with the right-sided tissue, which reflects the effect of cell shape change. Using a boundary condition in which part of the dorsal midline was fixed (see STAR Methods about boundary conditions), we solved our mechanical model using a finite-element method (for a detailed description of the calculation method, see Kida and Morishita, 2018). Simulation under these conditions reproduced the initiation phase, i.e., rightward shift and C-shaped change of the LR boundary, without significant rotation of the tube as was described in the previous section and as was also observed in explant cultures (Figure 2; Video S6). This result supports the sufficiency of the LR asymmetric response to tissue stress as a minimal condition for the initiation of C-shaping, i.e., spatial constraints at the anterior/posterior boundary assumed for the physical buckling model are not necessary. However, our simulation has not yet reproduced the full process of C-looping shown in Figure 2C and Video S1. Development of a model that can handle 3D large deformation will be necessary to fully understand what drives the C-looping. We will also need to consider the effects of constraints and forces at the boundaries, which might be important for the later helical looping process (Voronov et al., 2004; Kidokoro et al., 2008; Le Garrec et al., 2017).

DISCUSSION

Our quantitative analysis of tissue deformation dynamics revealed the LR asymmetry in the direction of deformation anisotropy within the myocardial tube. The tissue elongates longitudinally in the right side of the heart tube and more circumferentially in the left side. We also showed that directional cell rearrangement observed in the right side of the heart tube is a key process for achieving LR asymmetric tissue deformation. These findings are inconsistent with behaviors assumed in previous models. Our data on cell trajectories and quantified tissue deformation map showed that little ventral bending occurs during the C-shaping of the heart tube, and that the LR boundary of the heart tube shifts rightward not because of a simple rigid body rotation assumed in the ventral bending and rotation model, but instead the C-shaped tube is achieved by the combination of circumferential deformation of the left tissue and longitudinal deformation of the right tissue. This LR asymmetry in the direction of tissue deformation is also not assumed in the physical buckling model. In most simulations of the buckling model, the direction of maximum principal strain (i.e., direction of tissue elongation) is along the longitudinal axis in both left- and right-sided heart tubes. Moreover, no previous models assumed that dynamic cell rearrangement within the tube itself, rather than at the tube boundaries (or OVs), makes a significant contribution to tissue deformation. Together, this study provides integrated knowledge about morphogenetic mechanisms at the tissue and cellular scales for C-looping of the heart tube.

On the other hand, what gives directional information to cells and what generates the LR asymmetry in cell behaviors remain open questions. Here we hypothesized that left- and right-sided tissues show different cellular responses to stress wherein longitudinal tissue elongation through directional cell rearrangement occurs only in right-sided tissue. Although the molecular mechanisms that cause this LR asymmetry await further characterization, the expression patterns of many genes in heart tissue show clear LR asymmetry, and knockouts of several of these genes abolish looping and produce heart malformation (Kathiriya and Srivastava, 2000; Kirby, 2007). Thus, identification of which genes regulate cell rearrangement during heart tube looping is needed. For instance, a recent report showed that activation of protein kinase C (PKC) signaling frequently causes leftward looping, suggesting a possible role for PKC signaling in determining the LR asymmetry of cellular behavior (Ray et al., 2018). The epithelial-mesenchymal transition (EMT)-related factor Prrx1 also affects the direction of looping (Ocaña et al., 2017). Ocaña et al. (2017) observed in zebrafish embryos that LR asymmetry in cell motility at the posterior pole of the heart tube (not within the tube itself) caused by LR asymmetric Prrx1 gene expression induces a leftward shift of the posterior pole. However, whether and how this shift relates to the C-looping process is still unknown. Because Prrx1expression is lost once cells join the tube, Prrx1 likely does not directly cause directional cell rearrangement within the right-sided tube.

In addition to LR patterning genes, actin-associated (or actin-related) genes could be critical factors for C-looping. Here, we found that actin polymerization is required for directional cell rearrangement that achieves anisotropic tissue deformation, but details of intracellular mechanism, particularly how F-actin orientation through actin polymerization drives cell rearrangement, is unknown. Previous studies of organ/animal development showed that contractility arising from myosin-phosphorylation is important for cell rearrangement (Lu et al., 2008; Noël et al., 2013; Ocaña et al., 2017; Merks et al., 2018). However, other studies (Latacha et al., 2005; Nerurkar et al., 2006; Shi et al., 2014b) and our replication experiment suggested that, at least during chick heart development, myosin activity is not involved in cell rearrangement during C-looping. A recent study reporting myosin II-independent collective cell movement in the context of tracheal development in *Drosophila* showed that cell movement mainly depends on actin polymerization, and myosin activity is less important (Ochoa-Espinosa et al., 2017). The directional cell rearrangement observed

during heart looping might be driven by similar actin-dependent mechanisms underlying such collective cell migration.

On the right side of the heart tube, we found that rearrangement of cardiomyocytes occurs so that the tissue shrinks along the direction of the long axis of the cell, and thus tissue elongates perpendicularly to the direction of cell shape. Similar processes have been reported for other organs/animals, such as neuroepithelial cells during optic vesicle protrusion and neural tube closure in chicks (Nishimura et al., 2012; Morishita et al., 2017) and notochord convergent extension in *Xenopus* (Shindo and Wallingford, 2014). Conditions for achieving such orthogonality between tissue/cell behaviors have also been examined with a mathematical model (Ishihara et al., 2017). These findings suggest that this relationship between tissue and cellular processes is a well-preserved mechanism that underlies the initial development of different organs.

As we showed here, through quantification and comparison of tissue- and cellular-level dynamics, the contributions of each cellular process to tissue deformation or tissue morphogenesis can be elucidated. Currently, organs for which full dynamics have been quantitatively described are limited, and this is particularly true for organs that have complex 3D structures. The analytical approaches adopted here can be applied to different systems beyond heart development to reveal universal design principles of organ morphogenesis.

STAR★METHODS

Detailed methods are provided in the online version of this paper and include the following:

- KEY RESOURCES TABLE
- LEAD CONTACT AND MATERIALS AVAILABILITY
- EXPERIMENTAL MODEL AND SUBJECT DETAILS
  - Embryos and culture preparations
  - Embryo stages focused on in this study
- METHOD DETAILS
  - Electroporation
  - Immunofluorescence
  - 3-D live imaging
  - Pharmaceutical treatment to inhibit cell cycle/actin polymerization/myosin phosphorylation
- QUANTIFICATION AND STATISTICAL ANALYSIS
  - Reconstruction of tissue deformation maps
  - Coordinate systems in data analyses
  - Quantification of cell geometry
  - Quantification of cell rearrangement
  - Quantification of F-actin orientation
  - Mechanical simulation to calculate stress distribution on the heart tube
  - Mechanical simulation for morphogenesis with stress-dependent active deformation
  - Data processing
- DATA AND CODE AVAILABILITY

SUPPLEMENTAL INFORMATION

Supplemental Information can be found online at https://doi.org/10.1016/j.celrep.2020.02.071.

ACKNOWLEDGMENTS

This work was supported by grants from the Ministry of Education, Culture, Sports, Science and Technology of Japan (17H01819 to Y.M.) and from the PRESTO (Precursory Research for Embryonic Science and Technology) program of Japan Science and Technology Agency (to Y.M.). N. Kawahira was a fellow of the Takeda Science Foundation. We thank T. Suzuki for providing plasmids containing fluorescent protein gene.

AUTHOR CONTRIBUTIONS

D.O. and Y.M. designed this study. N. Kawahira performed all experiments using chick embryos and data analysis for molecular and cellular dynamics. D.O. supervised experimental works. N. Kida performed continuum mechanical modeling and finite element simulations. K.H. helped with image data processing. Y.M. analyzed tissue deformation dynamics and supervised analytical work. All authors discussed the results. N. Kawahira and Y.M. wrote the paper.

DECLARATION OF INTERESTS

The authors declare no competing interests.

Received: December 19, 2018
Revised: August 1, 2019
Accepted: February 18, 2020
Published: March 17, 2020

REFERENCES

Aleksandrova, A., Czirok, A., Kosa, E., Galkin, O., Cheuvront, T.J., and Rongish, B.J. (2015). The endoderm and myocardium join forces to drive early heart tube assembly. Dev. Biol. *404*, 40–54.

Ambrosi, D., Ateshian, G.A., Arruda, E.M., Cowin, S.C., Dumais, J., Goriely, A., Holzapfel, G.A., Humphrey, J.D., Kemkemer, R., Kuhl, E., et al. (2011). Perspectives on biological growth and remodeling. J. Mech. Phys. Solids *59*, 863–883.

Auman, H.J., Coleman, H., Riley, H.E., Olale, F., Tsai, H.J., and Yelon, D. (2007). Functional modulation of cardiac form through regionally confined cell shape changes. PLoS Biol *5*, e53.

Baldwin, H.S., and Solursh, M. (1989). Degradation of hyaluronic acid does not prevent looping of the mammalian heart in situ. Dev. Biol *136*, 555–559.

Bayraktar, M., and Männer, J. (2014). Cardiac looping may be driven by compressive loads resulting from unequal growth of the heart and pericardial cavity. Observations on a physical simulation model. Front. Physiol *5*, 112.

Bertet, C., Sulak, L., and Lecuit, T. (2004). Myosin-dependent junction remodelling controls planar cell intercalation and axis elongation. Nature *429*, 667–671.

Blanchard, G.B., Kabla, A.J., Schultz, N.L., Butler, L.C., Sanson, B., Gorfinkiel, N., Mahadevan, L., and Adams, R.J. (2009). Tissue tectonics: morphogenetic strain rates, cell shape change and intercalation. Nat. Methods *6*, 458–464.

Chapman, S.C., Collignon, J., Schoenwolf, G.C., and Lumsden, A. (2001). Improved method for chick whole-embryo culture using a filter paper carrier. Dev. Dyn. *220*, 284–289.

Cignoni, P., Callieri, M., Corsini, M., Dellepiane, M., Ganovelli, F., and Ranzug, G. (2008). MeshLab: an open-source mesh processing tool. In Proccedings of the 6th Eurographics Italian Chapter Conference 2008, V. Scarano, R. De Chiara, and U. Err, eds. (The Eurographics Association), pp. 129–136.

Conte, V., Muñoz, J.J., and Miodownik, M. (2008). A 3D finite element model of ventral furrow invagination in the Drosophila melanogaster embryo. J. Mech. Behav. Biomed. Mater. *1*, 188–198.

Davidson, L.A., and Keller, R.E. (1999). Neural tube closure in Xenopus laevis involves medial migration, directed protrusive activity, cell intercalation and convergent extension. Development *126*, 4547–4556.

Doube, M., Kłosowski, M.M., Arganda-Carreras, I., Cordelières, F.P., Dougherty, R.P., Jackson, J.S., Schmid, B., Hutchinson, J.R., and Shefelbine, S.J. (2010). BoneJ: Free and extensible bone image analysis in ImageJ. Bone *47*, 1076–1079.

Evans, S.M., Yelon, D., Conlon, F.L., and Kirby, M.L. (2010). Myocardial lineage development. Circ. Res. *107*, 1428–1444.

Filas, B.A., Efimov, I.R., and Taber, L.A. (2007). Optical coherence tomography as a tool for measuring morphogenetic deformation of the looping heart. Anat. Rec. (Hoboken) *290*, 1057–1068.

Ghaskadbi, S., and Mulherkar, L. (1984). Effects of cytochalasin H on chick embryo explants cultured in vitro. Toxicology *33*, 323–330.

Guillot, C., and Lecuit, T. (2013). Mechanics of epithelial tissue homeostasis and morphogenesis. Science *340*, 1185–1189.

Guirao, B., Rigaud, S.U., Bosveld, F., Bailles, A., López-Gay, J., Ishihara, S., Sugimura, K., Graner, F., and Bellaïche, Y. (2015). Unified quantitative characterization of epithelial tissue development. eLife *4*, e08519.

Hamburger, V., and Hamilton, H.L. (1951). A series of normal stages in the development of the chick embryo. J. Morphol *88*, 49–92.

Hoogaars, W.M.H., Barnett, P., Moorman, A.F., and Christoffels, V.M. (2007a). T-box factors determine cardiac design. Cell. Mol. Life Sci. *64*, 646–660.

Hoogaars, W.W.M.H., Christoffels, V.M., and Moorman, A.F.M. (2007b). Morphogenesis of the Vertebrate Heart. Adv. Dev. Biol. *18*, 31–68.

Ishihara, S., Marcq, P., and Sugimura, K. (2017). From cells to tissue: A continuum model of epithelial mechanics. Phys. Rev. E *96*, 022418.

Itasaki, N., Nakamura, H., Sumida, H., and Yasuda, M. (1991). Actin bundles on the right side in the caudal part of the heart tube play a role in dextro-looping in the embryonic chick heart. Anat. Embryol. (Berl.) *183*, 29–39.

Itasaki, N., Nakamura, H., and Yasuda, M. (1989). Changes in the arrangement of actin bundles during heart looping in the chick embryo. Anat. Embryol. (Berl.) *180*, 413–420.

Kathiriya, I.S., and Srivastava, D. (2000). Left-right asymmetry and cardiac looping: Implications for cardiac development and congenital heart disease. Am. J. Med. Genet. *97*, 271–279.

Kida, N., and Adachi, T. (2015). Finite element formulation and analysis for an arterial wall with residual and active stresses. Comput. Methods Biomech. Biomed. Engin. *18*, 1143–1159.

Kida, N., and Morishita, Y. (2018). Continuum mechanical modeling of developing epithelial tissues with anisotropic surface growth. Finite Elem. Anal. Des. *144*, 49–60.

Kidokoro, H., Okabe, M., and Tamura, K. (2008). Time-lapse analysis reveals local asymmetrical changes in C-looping heart tube. Dev. Dyn. *237*, 3545–3556.

Kidokoro, H., Yonei-Tamura, S., Tamura, K., Schoenwolf, G.C., and Saijoh, Y. (2018).). The heart tube forms and elongates through dynamic cell rearrangement coordinated with foregut extension. Development *145*, dev152488.

Kirby, M.L. (2007). Cardiac Development (Oxford University Press).

Latacha, K.S., Rémond, M.C., Ramasubramanian, A., Chen, A.Y., Elson, E.L., and Taber, L.A. (2005). Role of actin polymerization in bending of the early heart tube. Dev. Dyn. *233*, 1272–1286.

Le Garrec, J.F., Domínguez, J.N., Desgrange, A., Ivanovitch, K.D., Raphaël, E., Bangham, J.A., Torres, M., Coen, E., Mohun, T.J., and Meilhac, S.M. (2017). A predictive model of asymmetric morphogenesis from 3D reconstructions of mouse heart looping dynamics. eLife *6*, e28951.

Legland, D., Arganda-Carreras, I., and Andrey, P. (2016). MorphoLibJ: integrated library and plugins for mathematical morphology with ImageJ. Bioinformatics *32*, 3532–3534.

Lenhart, K.F., Holtzman, N.G., Williams, J.R., and Burdine, R.D. (2013). Integration of nodal and BMP signals in the heart requires FoxH1 to create left-right differences in cell migration rates that direct cardiac asymmetry. PLoS Genet. *9*, e1003109.

Lu, W., Seeholzer, S.H., Han, M., Arnold, A.S., Serrano, M., Garita, B., Philp, N.J., Farthing, C., Steele, P., Chen, J., and Linask, K.K. (2008). Cellular non-muscle myosins NMHC-IIA and NMHC-IIB and vertebrate heart looping. Dev. Dyn. *237*, 3577–3590.

Manasek, F.J., Burnside, B., and Stroman, J. (1972a). The sensitivity of developing cardiac myofibrils to cytochalasin-B (electron microscopy-polarized light-Z-bands-heartbeat). Proc. Natl. Acad. Sci. USA *69*, 308–312.

Manasek, F.J., Burnside, M.B., and Waterman, R.E. (1972b). Myocardial cell shape change as a mechanism of embryonic heart looping. Dev. Biol. *29*, 349–371.

Manasek, F.J., and Monroe, R.G. (1972). Early cardiac morphogenesis is independent of function. Dev. Biol. *27*, 584–588.

Männer, J. (2000). Cardiac looping in the chick embryo: a morphological review with special reference to terminological and biomechanical aspects of the looping process. Anat. Rec. *259*, 248–262.

Meilhac, S.M., Esner, M., Kerszberg, M., Moss, J.E., and Buckingham, M.E. (2004). Oriented clonal cell growth in the developing mouse myocardium underlies cardiac morphogenesis. J. Cell Biol. *164*, 97–109.

Merks, A.M., Swinarski, M., Meyer, A.M., Müller, N.V., Özcan, I., Donat, S., Burger, A., Gilbert, S., Mosimann, C., Abdelilah-Seyfried, S., and Panáková, D. (2018). Planar cell polarity signalling coordinates heart tube remodelling through tissue-scale polarisation of actomyosin activity. Nat. Commun. *9*, 2161.

Moorman, A.F.M., and Christoffels, V.M. (2003). Cardiac chamber formation: development, genes, and evolution. Physiol. Rev. *83*, 1223–1267.

Morishita, Y., Hironaka, K.I., Lee, S.W., Jin, T., and Ohtsuka, D. (2017). Reconstructing 3D deformation dynamics for curved epithelial sheet morphogenesis from positional data of sparsely-labeled cells. Nat. Commun. *8*, 15.

Nerurkar, N.L., Ramasubramanian, A., and Taber, L.A. (2006). Morphogenetic adaptation of the looping embryonic heart to altered mechanical loads. Dev. Dyn. *235*, 1822–1829.

Nishimura, T., Honda, H., and Takeichi, M. (2012). Planar cell polarity links axes of spatial dynamics in neural-tube closure. Cell *149*, 1084–1097.

Noël, E.S., Verhoeven, M., Lagendijk, A.K., Tessadori, F., Smith, K., Choorapoikayil, S., den Hertog, J., and Bakkers, J. (2013). A Nodal-independent and tissue-intrinsic mechanism controls heart-looping chirality. Nat. Commun. *4*, 2754.

Ocaña, O.H., Coskun, H., Minguillón, C., Murawala, P., Tanaka, E.M., Galcerán, J., Muñoz-Chápuli, R., and Nieto, M.A. (2017). A right-handed signalling pathway drives heart looping in vertebrates. Nature *549*, 86–90.

Ochoa-Espinosa, A., Harmansa, S., Caussinus, E., and Affolter, M. (2017). Myosin II is not required for *Drosophila* tracheal branch elongation and cell intercalation. Development *144*, 2961–2968.

Patten, B.M. (1922). The formation of the cardiac loop in the chick. Am. J. Anat. *30*, 373–397.

Pellegrin, S., and Mellor, H. (2007). Actin stress fibres. J. Cell Sci. *120*, 3491–3499.

Pestel, J., Ramadass, R., Gauvrit, S., Helker, C., Herzog, W., and Stainier, D.Y. (2016). Real-time 3D visualization of cellular rearrangements during cardiac valve formation. Development *143*, 2217–2227.

Ray, P., Chin, A.S., Worley, K.E., Fan, J., Kaur, G., Wu, M., and Wan, L.Q. (2018). Intrinsic cellular chirality regulates left-right symmetry breaking during cardiac looping. Proc. Natl. Acad. Sci. USA *115*, E11568–E11577.

Rosenquist, G.C., and DeHaan, R.L. (1966). Migration of Precardiac Cells in the Chick Embryo: A Radioautographic Study (Carnegie Institution of Washington).

Rueden, C.T., Schindelin, J., Hiner, M.C., DeZonia, B.E., Walter, A.E., Arena, E.T., and Eliceiri, K.W. (2017). ImageJ2: ImageJ for the next generation of scientific image data. BMC Bioinform. *18*, 529.

Savin, T., Kurpios, N.A., Shyer, A.E., Florescu, P., Liang, H., Mahadevan, L., and Tabin, C.J. (2011). On the growth and form of the gut. Nature *476*, 57–62.

Schindelin, J., Arganda-Carreras, I., Frise, E., Kaynig, V., Longair, M., Pietzsch, T., Preibisch, S., Rueden, C., Saalfeld, S., Schmid, B., et al. (2012). Fiji: an open-source platform for biological-image analysis. Nat. Methods *9*, 676–682.

Schneider, C.A., Rasband, W.S., and Eliceiri, K.W. (2012). NIH Image to ImageJ: 25 years of image analysis. Nat. Methods *9*, 671–675.

Shen, L., Farid, H., and McPeek, M.A. (2009). Modeling three-dimensional morphological structures using spherical harmonics. Evolution *63*, 1003–1016.

Shi, Y., Yao, J., Xu, G., and Taber, L.A. (2014b). Bending of the looping heart: differential growth revisited. J. Biomech. Eng. *136*, 081002.

Shi, Y., Yao, J., Young, J.M., Fee, J.A., Perucchio, R., and Taber, L.A. (2014a). Bending and twisting the embryonic heart: a computational model for c-looping based on realistic geometry. Front. Physiol. *5*, 297.

Shindo, A., and Wallingford, J.B. (2014). PCP and septins compartmentalize cortical actomyosin to direct collective cell movement. Science *343*, 649–652.

Smith, K.A., Chocron, S., von der Hardt, S., de Pater, E., Soufan, A., Bussmann, J., Schulte-Merker, S., Hammerschmidt, M., and Bakkers, J. (2008). Rotation and asymmetric development of the zebrafish heart requires directed migration of cardiac progenitor cells. Dev. Cell *14*, 287–297.

Soufan, A.T., van den Berg, G., Ruijter, J.M., de Boer, P.A., van den Hoff, M.J., and Moorman, A.F. (2006). Regionalized sequence of myocardial cell growth and proliferation characterizes early chamber formation. Circ. Res. *99*, 545–552.

Stalsberg, H. (1969). Regional mitotic activity in the precardiac mesoderm and differentiating heart tube in the chick embryo. Dev. Biol. *20*, 18–45.

Tallinen, T., Chung, J., Rousseau, F., Girard, N., and Lefèvre, J., and Mahadevan, L.. (2016). On the growth and form of cortical convolutions. Nat. Phys. *12*, 588–593.

Tanaka, J., Harada, H., Ito, K., Ogura, T., and Nakamura, H. (2010). Gene manipulation of chick embryos in vitro, early chick culture, and long survival in transplanted eggs. Dev. Growth Differ. *52*, 629–634.

Voronov, D.A., Alford, P.W., Xu, G., and Taber, L.A. (2004). The role of mechanical forces in dextral rotation during cardiac looping in the chick embryo. Dev. Biol. *272*, 339–350.

Wozniak, M.A., and Chen, C.S. (2009). Mechanotransduction in development: a growing role for contractility. Nat. Rev. Mol. Cell Biol. *10*, 34–43.

Yuan, D., and He, P. (2012). Vascular remodeling alters adhesion protein and cytoskeleton reactions to inflammatory stimuli resulting in enhanced permeability increases in rat venules. J. Appl. Physiol. *113*, 1110–1120.

Yue, Q., Wagstaff, L., Yang, X., Weijer, C., and Münsterberg, A. (2008). Wnt3a-mediated chemorepulsion controls movement patterns of cardiac progenitors and requires RhoA function. Development *135*, 1029–1037.

STAR★METHODS

KEY RESOURCES TABLE

REAGENT or RESOURCE	SOURCE	IDENTIFIER
Antibodies		
Rat monoclonal anti-GFP	Nacalai Tesque	Cat# GF090R; RRID: AB_2314545
Rabbit polyclonal anti-Histone H3, phospho (Ser10)	Millipore	Cat# 06-570; RRID: AB_310177
Goat anti-Rat Alexa Fluor-conjugated antibody	Thermo Fisher Scientific	Cat# A-11006; RRID: AB_2534074
Goat anti-Rabbit Alexa Fluor-conjugated antibody	Thermo Fisher Scientific	Cat# A-11036; RRID: AB_10563566
Chemicals, Peptides, and Recombinant Proteins		
Aphidicolin	Wako	011-09811
Alexa Fluor 488 Phalloidin	Thermo Fisher Scientific	A12379
Alexa Fluor 568 Phalloidin	Thermo Fisher Scientific	A12380
Blebbistatin	Sigma-Aldrich	B5002-100MG
Calyculin A	Wako	038-14453
Cytochalasin D	Wako	037-17561
DMSO	Sigma-Aldrich	D2650-5X5ML
FM4-64FX	Thermo Fisher Scientific	F34653
Fluoroshield with DAPI	ImmunoBioScience	AR-6501-02
FxCycle PI/RNase Staining Solution	Thermo Fisher Scientific	F10797
Hoechst33342	Thermo Fisher Scientific	H3570
Y27632	Wako	257-00513
Critical Commercial Assays		
Click-iT EdU Alexa Fluor 488 Imaging Kit	Thermo Fisher Scientific	C10337
Deposited Data		
Quantified data from microscopic images	This paper	https://doi.org/10.17632/kk3gw6cx7p.1
Experimental Models: Organisms/Strains		
Fertilized chicken egg	Shiroyama Farm, Inoue Egg Farm	N/A
Recombinant DNA		
pCAGGS-H2B-EGFP	Dr. T. Suzuki	N/A
pCAGGS-EGFPF-2A-EGFP	Dr. T. Suzuki	N/A
Software and Algorithms		
ImageJ/Fiji (ver. 2.0.0-rc-69/1.52i)	Schindelin et al., 2012	RRID: SCR_002285
Imaris (ver. 7.6.5)	Bitplane	RRID: SCR_007370
Meshlab (v2016.12)	Cignoni et al., 2008	http://www.meshlab.net
Mathematica (version 11)	Wolfram Research	RRID: SCR_014448
Python (2.7.12)	Python.org	RRID: SCR_008394
R (3.5.1)	R project	RRID: SCR_001905
SPHARM Morphogenetic Software	Shen et al., 2009	http://www.enallagma.com/SPHARM.php

LEAD CONTACT AND MATERIALS AVAILABILITY

This study did not generate new unique reagents. Further information and requests for resources and reagents should be directed to and will be fulfilled by the Lead Contact, Yoshihiro Morishita (yoshihiro.morishita@riken.jp).

EXPERIMENTAL MODEL AND SUBJECT DETAILS

Embryos and culture preparations

Fertilized chicken eggs (Shiroyama Farm and Inoue Egg Farm) were incubated at 38°C in a humidified incubator until the embryos reach the appropriate stages (Hamburger and Hamilton, 1951). For each experiment, embryos were transplanted using the EC culture method (Chapman et al., 2001). All the animal experiments were performed under the ethical guidelines of RIKEN Center for Biosystems Dynamics Research.

Embryo stages focused on in this study

As described in Introduction, C-looping is the first event in heart development that shows left-right asymmetry in appearance. In the chick development, C-looping is commonly said to occur during a period from Hamburger and Hamilton (HH) stage 9+/10- to HH11+/12 (Figure 1A). Figure 1D shows a typical morphological change that we focused on in this study, covering nearly the entire C-looping process (see also Video S7). Morphological changes after HH12, i.e., more helical shaping including S-looping, are difficult to image at high resolution, which precludes objective discussion of morphogenetic processes.

METHOD DETAILS

Electroporation

HH3/3+ embryos were prepared for *in vitro* electroporation to label prospective cardiomyocytes in the heart tube. Plasmids were electroporated into epiblast cells at gastrulation near the primitive node (Tanaka et al., 2010). The electroporation conditions were: one poration pulse of 6V, 10 ms and five 3 V driving pulses, 50 ms with interval of 50 ms. These pulses were charged twice using a CUY21EX electroporator (BEX CO. Ltd). After manipulation, embryos were incubated at 38°C with 5% CO_2.

Immunofluorescence

Chick embryos were fixed in 4% PFA/PBS overnight and then rinsed in PBS (TaKaRa PBS tablets T900). The vitelline membrane and splanchnopleura were then removed to expose the heart tube for better staining and visualization. For permeabilization, the embryos were incubated with 1% Triton X-100 (Nacalai Tesque) in PBS for 1 h and washed with 0.2% PBST (Tween-20, Wako, 166-21213) three times. For antibody reactions, embryos were incubated overnight with the primary antibody (see below), washed extensively, and then incubated overnight with a secondary antibody. After the antibody reactions, nuclei or F-actin were stained using propidium iodide (Thermo Fisher F10797) or Alexa Fluor 488/568 phalloidin (Thermo Fisher A12379, A12380). The antibodies used for immunostaining were: anti-GFP rat IgG2 monoclonal antibody (Nacalai Tesque, GF090R) 1:1,000, Anti-phospho-Histone H3 (Ser10) Antibody (Millipore, 06-570) 1:500, anti-rat Alexa Fluor-conjugated goat antibody (Thermo Fisher, A11006) 1:5,000, anti-rabbit Alexa Fluor-conjugated antibody (Thermo Fisher, A11036) 1:5,000. All procedures were performed at room temperature.

3-D live imaging

3-D live imaging was performed using an upright microscope (FV1000MPE; Olympus) equipped with an Olympus 25 × /NA1.05 XLPLN25XWMP objective lens and a multi-photon femtosecond laser (excitation wavelength 920 nm; Mai-Tai DeepSeeHP, Spectra-Physics). Embryos in which cardiomyocytes were sparsely labeled were prepared. The embryos were electroporated with pCAGGS-H2B-EGFP expression vector and incubated. Before live imaging, cell membranes were stained with 80 μl of FM4-64FX lipophilic dye (10 ng/μl, Thermo Fisher) for 1 h. The embryos were then immersed in PBS, and 3-D heart morphology was obtained as a Z stack of optical sectional images (80 slices with an interval of 2.5 μm; each slice was 512 × 512 pixels). In later stages, four X-Y tiles were obtained to cover the entire heart tube region. After imaging, the embryos were returned to the incubator until the next imaging time point. Within each time interval (2 h), embryo development progressed to the next somite stage. Although this developmental speed is slightly slower than that in normal development (1.5 h/somite), the morphology itself was normal. All images were taken at room temperature.

Pharmaceutical treatment to inhibit cell cycle/actin polymerization/myosin phosphorylation

The role of actin polymerization, myosin phosphorylation, and cell division were assessed following: i) Cytochalasin D (Wako 037-17561; final concentration 5 μM) or Latrunculin A (Wako 125-04363; 5 μM) treatment to inhibit actin polymerization; ii) Blebbistatin (Sigma-Aldrich B5002-100MG; 100 μM), Y27632 (Wako 257-00513; 100 μM) or Calyculin A (Wako 038-14453; 100 nM) treatment to alter myosin phosphorylation; or iii) aphidicolin (Wako 011-09811; 100 μM) treatment to inhibit cell cycle progression. These reagents were dissolved in DMSO to produce a stock solution, and then diluted to the final concentration in PBS just before use. The reagents (100 μl) were gently applied to whole chick embryos in EC culture at HH10. DMSO diluted in PBS with the respective final concentration was used in the control experiments. Embryos were fixed at the corresponding stages and processed for immunostaining as described above (Figure S2).

QUANTIFICATION AND STATISTICAL ANALYSIS

Reconstruction of tissue deformation maps

Bayesian reconstruction of tissue deformation maps of the myocardium during C-looping was performed as we previously described (Morishita et al., 2017). In the method, 3-D and 2-D representations of the entire heart tube and landmark cells (i.e., GFP-positive cells) are needed. In order to obtain the 3-D morphology, we first manually traced the basal surface of myocardium for each section along different axes. By stacking the traced data, the 3-D morphology of the basal surface was reconstructed. The 3-D model of the myocardium and 2-D coordinates on it were obtained using the spherical harmonics expansion (SHE). The positions of GFP-expressing cardiomyocytes before and after deformation were manually linked, and their 2-D coordinates were obtained by projecting them onto the approximated surface by SHE. The reconstruction of deformation map was performed for three embryos, and the numbers of labeled cells used for the reconstruction were 179, 78, and 126, respectively. Mean residual errors for the three embryos are 9.39, 6.77, and 11.0 μm, respectively.

Coordinate systems in data analyses

To quantify/compare the orientations of different variables at different spatial scales such as tissue deformation anisotropy, cell shape/rearrangement, and F-actin, we must define coordinate systems on the curved myocardial surface. Although we used SHE-based (2-D) coordinates in the Bayesian reconstruction of the tissue deformation map for analytical convenience, another coordinate system more reflecting tube morphologies (in particular, longitudinal, circumferential, and apical-basal axes) defined below was introduced in the quantification/comparison of the orientation of each variable.

First, the anterior and posterior ends in a polygon model of heart tube were determined. Then, using the "Generate scalar harmonic field" command in Meshlab software (Cignoni et al., 2008), a harmonic field (different from SHE) was set using those anterior and posterior ends as boundary conditions. This scalar field yields a spatial distribution of a scalar variable similar to that seen in heat conduction, i.e., the polygon was "heated" at the anterior end and "cooled" at the posterior ends; thus, the value of the variable shows a gradual decrease toward the posterior end. Based on this harmonic scalar field, at each point on the heart tube, the longitudinal direction was defined as the gradient direction of the scalar, and the circumferential direction as its contour direction (Figure S1D). Then, the normal (i.e., apico-basal) direction was defined so as to be perpendicular to the myocardial surface. These three directions provide an orthogonal coordinate system for each point on the heart tube.

Quantification of cell geometry

Cardiomyocyte shape was visualized using GFP protein expressed in the cytoplasm and cell membrane by the pCAGGS-EGFPF-2A-EGFP plasmid. The plasmid was electroporated into the cells as described above; GFP-positive cardiomyocytes were sparsely distributed in the heart tube. The cardiomyocytes were further immunostained by anti-GFP rat IgG2 monoclonal antibody (Nacalai Tesque, GF090R), and nuclei were counterstained by PI that could be used to distinguish two adjacent cardiomyocytes. 3-D volumetric image data were obtained using the same microscope equipment described above. In this case, an additional laser was used for multi-wavelength excitation (excitation wavelength 1040 nm; HighQ2 laser, Spectra-Physics), and the Z stack was taken using 1 × 1 x 1 μm^3 voxel sizes. Each cell shape was quantified using ImageJ/Fiji software (Schindelin et al., 2012; Rueden et al. 2017; Schneider et al., 2012). Cardiomyocyte contours were traced manually using freehand selections in each Z-slice, and 3-D binary images representing all segmented cell shapes were created. These 3-D cell shapes were quantified using "Particle Analysis 3D" in the MorpholibJ plugin (Legland et al., 2016). To calculate statistics, each cell shape was approximated as a 3-D ellipsoid calculated by MorpholibJ (Figure S3A). The cell height was defined as the length when the 3-D ellipsoid was projected onto the AB axis, and the cell area on the longitudinal-circumferential (LC) plane was defined as the area of the 2-D ellipse in the LC cross section through the cell centroid of the 3-D ellipsoid (Figure 3C).

Quantification of cell rearrangement

To visualize cellular movement in the heart tube, chick embryos at HH10 were prepared using the EC culture technique. The nuclei were stained with Hoechst 33342 dye (Thermo Fisher Scientific H3570) that was diluted 500-fold in high potassium solution (140 mM KCl and 14 mM NaCl in phosphate buffer) (Manasek and Monroe, 1972; Filas et al., 2007) to attenuate the heartbeat, because myocardial contraction impairs precise acquisition of live imaging data. 1-2 μl of Hoechst solution were injected into the pericardial cavity through the splanchnopleura using a pulled glass capillary. After a 30-min incubation, the embryo was moved to a glass-bottom dish coated with a thin layer of EC culture medium (dorsal-side up), and then all nuclei in the heart were live imaged every 5-15 min using a two-photon microscope equipped with a stage-top incubator.

To quantify the contribution of cell rearrangement or cell shape changes to tissue deformation during morphogenesis that occurs between HH10 and HH11, we adopted the method proposed by Blanchard et al. (2009). The tissue velocity gradient tensor ($\mathbf{L}_T$) was calculated from time lapse imaging data on the trajectories of cells included in the focal myocardial patch. The quantity called cell shape strain rate tensor ($\mathbf{L}_C$) that represents the change in cell shape was calculated from the information of the average cell shape on the right/left tissue obtained from cell geometry analysis (Figure 3). Using these values and the conditions $\mathrm{tr}\dot{\mathbf{E}}_T = \mathrm{tr}\dot{\mathbf{E}}_C$ and $\Omega_T = \Omega_C$, the strain rate tensor for cell rearrangement $\mathbf{L}_R$ was calculated, where $\dot{\mathbf{E}}_T$, $\dot{\mathbf{E}}_C$, Ω_T and Ω_C are tissue strain rate tensor, symmetrical cell

shape strain rate tensor, tissue spin, average cell spin, and the relationship $\mathbf{L}_{\cdot} = \dot{\mathbf{E}}_{\cdot} + \Omega_{\cdot}$ ($\cdot$ = T or C) holds. Note that $\mathbf{L}_R$ is the same tensor as one called intercalation strain rate tensor in the study by Blanchard et al. (2009).

Quantification of F-actin orientation

To visualize the orientation of F-actin structure in the heart tube, embryos at from HH10 to HH12 were prepared for phalloidin staining. After fixation and washing, embryos were incubated in Alexa Fluor 488 or 568 Phalloidin (Thermo Fisher A12379, A12380; diluted 1:1,000) for 1 h at room temperature. 3-D volumetric images were taken using the same settings as described above. F-actin structural anisotropy was quantified using ImageJ/Fiji software. F-actin signals in the heart region were extracted using masking images of the heart tube, then the small cubic region with a 60 μm edge length was cropped. After de-noising by median filter and scaling to isometric voxel size, a binary image was created using the Otsu method. The actin fiber orientation was quantified by "Anisotropy" in the BoneJ plugin (Doube et al., 2010). This quantification was repeated in multiple heart tube regions using simple macro scripting. After testing several image cropping sizes, we determined that 60 μm was sufficient to reflect consistent actin fiber orientations.

Mechanical simulation to calculate stress distribution on the heart tube

To calculate stress distribution on the heart tube, we modeled it as a thick-walled incompressible hyperelastic material with the strain energy function Ψ defined as:

$$\Psi = c(I_1 - 3) - p(J - 1),$$

$$c = 100 \ \ [\mathrm{kPa}],$$

where I_1 is the first invariant of the right Cauchy-Green strain tensor and $J = \det \boldsymbol{F}$. The scalar p indicates the indeterminate Lagrange multiplier. Using a finite element method, we numerically solved the mechanical balance under a small hydrostatic pressure with boundary conditions such that the anterior and posterior ends of the heart tube were fixed.

Mechanical simulation for morphogenesis with stress-dependent active deformation

To perform morphogenetic simulations under our hypothesis, we modeled the myocardial tissue as an actively deforming hyperelastic material. We adopted the constitutive law that the right-sided tissue actively elongates (assuming cell rearrangement on a cellular scale) perpendicular to the direction of maximum principal stress originating from hydrostatic pressure within the heart tube, while the left-sided tissue elongates (mainly through changes in cell shape) parallel to the direction of stress (see the main text). Note that the latter rule for the left-sided tissue is not essential to support our hypothesis. As a boundary condition, we fixed part of the dorsal midline position; from a biological perspective, this corresponds to the observation that the heart tube adheres to the dorsal mesocardium at its dorsal midline during the initial phase of C-looping. From a technical perspective, part of the tissue must be fixed to avoid rigid body motion. We tested several conditions in which one third of the anterior, middle or posterior of the dorsal midline was fixed. Some combinations of these regions were also fixed. All simulations returned qualitatively similar results, suggesting that the choice of boundary condition (i.e., which part of the dorsal midline is fixed) does not have a significant effect. The stress within the myocardium was assumed to be generated through a small hydrostatic pressure as stated above. To describe the constitutive law mathematically, we used multiplicative decomposition of the deformation gradient $\boldsymbol{F}$ into an active-deformation part $\boldsymbol{F}_g$ and an elastic part $\boldsymbol{F}_e$, i.e., $\boldsymbol{F} = \boldsymbol{F}_e\boldsymbol{F}_g$ (see Kida and Morishita, 2018 for details on mathematical formulation and numerical implementation). Specifically, we used the following functions for the right- and left-sided tissues, respectively;

$$\boldsymbol{F}_g^{(\mathrm{right})}(\theta_R) = \boldsymbol{N}_1 \otimes \boldsymbol{N}_1 + \theta_R \boldsymbol{N}_2 \otimes \boldsymbol{N}_2 + \frac{1}{\theta_R}\boldsymbol{N}_3 \otimes \boldsymbol{N}_3,$$

$$\boldsymbol{F}_g^{(\mathrm{left})}(\theta_L) = \boldsymbol{N}_1 \otimes \boldsymbol{N}_1 + \frac{1}{\theta_L}\boldsymbol{N}_2 \otimes \boldsymbol{N}_2 + \theta_L \boldsymbol{N}_3 \otimes \boldsymbol{N}_3,$$

where $\theta_R \equiv 1 + c_R t$ and $\theta_L \equiv 1 + c_L t$ are parameters for determining the rate of active deformation with the progression of computation time t (arbitrary time unit). In the simulation shown in Figure 6C, $c_R = 1.0$ and $c_L = 0.125$ were used. We also performed simulations using c_L values of 0, 0.25, 0.5 and 1 and confirmed that the simulation results were qualitatively unchanged. $\boldsymbol{N}_1$, $\boldsymbol{N}_2$, and $\boldsymbol{N}_3$ represent the unit vector for the direction of the minimum, intermediate, and maximum principal stresses at stage HH10 (before looping), respectively. The Moony-Rivlin type strain energy function was adopted (see Kida and Morishita, 2018).

Data processing

The orientation and morphological data quantified by ImageJ/Fiji were analyzed using "orientlib," "circular" and "movMF" packages in R (version 3.5.1). All data (except for data used in the reconstruction of tissue deformation maps) were described by the coordinate

systems defined above (i.e., longitudinal-circumferential-AB coordinates generated by the scalar harmonic field). The orientation data were treated as axial data in the calculation of mean angles and confidence intervals.

DATA AND CODE AVAILABILITY

Data used for the paper are publicly available from Mendeley Data at https://doi.org/10.17632/kk3gw6cx7p.1.